Geochemistry, Geophysics, Geosystems

RESEARCH ARTICLE
10.1029/2018GC007955

Special Section:
Magnetism in the Geosciences - Advances and Perspectives

A High-Resolution Geomagnetic Relative Paleointensity Record From the Arctic Ocean Deep-Water Gateway Deposits During the Last 60 kyr

Chiara Caricchi[1], Renata Giulia Lucchi[2], Leonardo Sagnotti[1], Patrizia Macrì[1], Alessio Di Roberto[3], Paola Del Carlo[3], Katrine Husum[4], Jan Sverre Laberg[5], and Caterina Morigi[6,7]

[1]Istituto Nazionale di Geofisica e Vulcanologia, Rome, Italy, [2]Istituto Nazionale di Oceanografia e di Geofisica Sperimentale, Sgonico, Italy, [3]Istituto Nazionale di Geofisica e Vulcanologia, Pisa, Italy, [4]Norwegian Polar Institute, Fram Centre, Tromsø, Norway, [5]Department of Geosciences, UIT-The Arctic University of Norway, Tromsø, Norway, [6]Dipartimento di Scienze della Terra, Università di Pisa, Pisa, Italy, [7]GEUS (Stratigraphy Department Geological Survey of Denmark and Greenland), Copenhagen, Denmark

Abstract We present a paleomagnetic and rock magnetic data set from two long sediment cores collected from Bellsund and Isfjorden contourite drifts located on the eastern side of the Fram Strait (western Spitsbergen margin). The data set gave the opportunity to define the behavior of the past geomagnetic field at high latitude and to constrain the palaeoclimatic events that occurred in a time framework spanning marine isotope stage 3 to the Holocene. A high-resolution age model was reconstructed by coupling 26 radiocarbon ages and high-resolution relative paleointensity and paleosecular variation of the geomagnetic field records for the last 60 kyr. We show the variation of the geomagnetic field at high latitudes, pointing out variability during periods of regular paleosecular variation (normal polarity) as well as during the most recent geomagnetic excursions, and we provide a high-resolution record of the Laschamps excursion. Cross-cores correlation allowed us to outline major, climate-related, sedimentary changes in the analyzed stratigraphic sequence that includes the meltwater events MWP-1a and MWP-19ky, and the Heinrich-like events H1, H2, H4, and H6. This contribution confirms that rock magnetic and paleomagnetic analysis can be successfully used as a correlation and dating tool for sedimentary successions at high latitudes, where accelerator mass spectrometry dates and oxygen isotope analyses are often difficult to obtain for the scarcity of calcareous microfossils and the uncertainties related to data calibration may be significant, as well as the complexity of water mass characteristics and dynamics through climate changes.

Key Points:
- Paleomagnetic and rock magnetic analyses of glaciomarine sequences
- Reconstruction of geomagnetic paleosecular variability at high latitudes (76 degrees to 77 degrees north)
- High-resolution correlation along eastern Fram Strait continental margin

Correspondence to:
C. Caricchi,
chiara.caricchi@ingv.it

Citation:
Caricchi, C., Lucchi, R. G., Sagnotti, L., Macrì, P., Di Roberto, A., Del Carlo, P., et al. (2019). A high-resolution geomagnetic relative paleointensity record from the Arctic Ocean deep-water gateway deposits during the last 60 kyr. *Geochemistry, Geophysics, Geosystems*, *20*, 2355–2377. https://doi.org/10.1029/2018GC007955

Received 11 SEP 2018
Accepted 3 APR 2019
Accepted article online 16 APR 2019
Published online 22 MAY 2019

1. Introduction

Temporal reconstruction of marine sedimentary successions is pivotal for the understanding of the mechanisms of sediment transport and dispersion on the continental slope in response to the late Quaternary climate changes and related glacial dynamics. However, at high latitude, as in the Arctic region, the chronostratigraphy of the sediments could be very challenging due to the paucity of datable material. Therefore, a multidisciplinary approach becomes essential for chronostratigraphy in order to precisely constrain the depositional processes and climatic events recorded in the sedimentary successions. In the last decades, several studies have suggested that reconstruction of the geomagnetic field relative paleointensity (RPI) variation could be successfully used as a valuable chronostratigraphic method for sediment dating and core correlation (e.g., Barletta et al., 2008; Caricchi et al., 2018; Guyodo & Valet, 1999; Kotilainen et al., 2000; Laj et al., 2000, 2004; Lisé-Pronovost et al., 2009; Sagnotti et al., 2011, 2016; St-Onge et al., 2003; Stoner et al., 2000, 2002, 2007; Tauxe, 1993; Valet & Meynadier, 1993; Yamazaki & Oda, 2005). Records of RPI can be used to better constrain the age of the deposits, especially for ages older than the range of confidence of traditional radiometric methods (e.g., ~58–62 kyr for ^{14}C radiocarbon dating).

At the same time, stratigraphic trends in rock magnetic parameters provide information on variation in the type, grain size, and concentration of magnetic minerals dispersed in the sediments, which are linked to depositional and environmental changes due to paleoclimatic and paleoceanographic variation (e.g., Blanchet et al., 2007; Brachfeld, 2006; Brachfeld et al., 2002, 2009; Hounslow & Morton, 2004; Kissel et al., 2003, 2008, 1999, 1997; Liu et al., 2012; Mazaud et al., 2002; Roberts et al., 2013; Rousse et al., 2006;

Stoner & Andrews, 1999; Thompson & Oldfield, 1986; Verosub & Roberts, 1995). Climate change exerts a strong control on continental weathering and erosional processes associated to the ice sheets dynamics. These processes determine the type of magnetic minerals and the rate of flux to the marine environment and its dilution with respect to the diamagnetic component (e.g., calcium carbonate and quartz) related to the bioproductivity, ice rafting, and wind/bottom currents transport. An important source of magnetic minerals is also represented by (i) the volcanic input of pyroclastic material (occurring as tephra layers in sedimentary sequences) during local explosive volcanic eruptions (whose products have a regional distribution), (ii) deposition of volcanic dust injected into the stratosphere from farsided volcanic events whose products have a global distribution, and (iii) from redistribution of volcanoclastic materials eroded from volcanic terrains.

Paleomagnetic and rock magnetic analyses are sensitive, high-resolution, rapid, and nondestructive methods, which can provide information about sedimentary variability that are strictly linked to the environmental condition providing information useful to determine (i) sediments source, (ii) rock magnetic stratigraphic trends for high-resolution cross-core correlation, and (iii) original constraints to develop age models for the sedimentary successions, providing a chronological framework for paleoenvironmental reconstructions.

We present paleomagnetic and rock magnetic data analyses on two long sediment cores collected with the Calypso-coring system from two contourite sediment drifts located on the eastern side of the Fram Strait (the Bellsund and Isfjorden sediment drifts, west of Spitsbergen, Rebesco et al., 2013), which represent the only deep-water gateway connecting the Arctic Ocean to the global ocean circulation. Paleomagnetic and rock magnetic data are coupled with radiocarbon ages and tephrostratigraphy for the setup of an original age model for the sediments recovered along the Northwestern Barents Sea and Eastern side of the Fram Strait. In addition, we reconstruct the RPI and paleosecular variation (PSV) records with very high resolution for the last 60 kyr BP comparing the records with the global geomagnetic field model SHA.DIF.14k (Pavón-Carrasco et al., 2014), GGF100k (Panovska et al., 2018), and the relative paleointensity stack GLOPIS-75 (Laj et al., 2004). This work also provides new information on the variation of the geomagnetic field at high latitudes, pointing out its variability during periods of regular PSV as well as during the most recent geomagnetic excursions.

2. Study Area

The study area is located along the southwestern margin of the Svalbard Archipelago (Figure 1). The morphology of this margin was shaped through time by the consecutive advances and retreats of the Svalbard-Barents Sea ice sheet in association with Late Quaternary climatic changes (Patton et al., 2017). According to Faleide et al. (1996), the onset of glacially dominated deposition along this margin occurred at about 2.3 Ma. However, shelf-edge glaciations started at only 1.5–1.3 Ma with direct deposition of glacigenic sediments on the upper slope (Butt et al., 2000). The sediments eroded from the onshore and offshore Svalbard substrate were delivered to the shelf break by fast flowing ice (ice streams) moving along cross-shelf glacial troughs (e.g., Mattingsdal et al., 2014). Highly consolidated detritus (glacigenic diamicton), delivered by the ice streams, was stacked on the upper slope promoting the oceanward progradation of the continental margin with the buildup of fan-shaped piles of detritus (Trough Mouth Fans, TMFs). According to Rebesco et al. (2013), the onset of the development of TMFs in this area of the western margin of Spitsbergen can be dated at about 1 Ma. In addition to glacigenic processes, the margin is influenced by persistent along slope bottom currents (contour currents, Eiken & Hinz, 1993; Jakobsson et al., 2007; see also Poirier & Hillaire-Marcel, 2011) whose depositional contribution is mainly observed during interglacials (Lucchi et al., 2013). Contour currents are responsible for the formation of contouritic drifts, which are mounded bathymetric features derived by sediment accumulation from persistent bottom currents active over millions of years. Contourite drifts are characterized by relatively high and continuous accumulation rates, in contrast to adjacent condensed hemipelagic/pelagic sequences, therefore representing suitable areas for high-resolution palaeoreconstructions (Rebesco et al., 2008, and references therein). Sediment drifts on the westernside of Svalbard occur in areas shielded from direct glacigenic input, such as between TMFs. Two minor contourite drifts (Bellsund and Isfjorden drifts) were identified on the seismic profiles collected along the western continental margin of Svalbard between 76° and 78°N, north of the Storfjorden glacial trough (Figure 2; Rebesco et al., 2013). The formation of such drifts, located at 1,500-m depth, was related to the

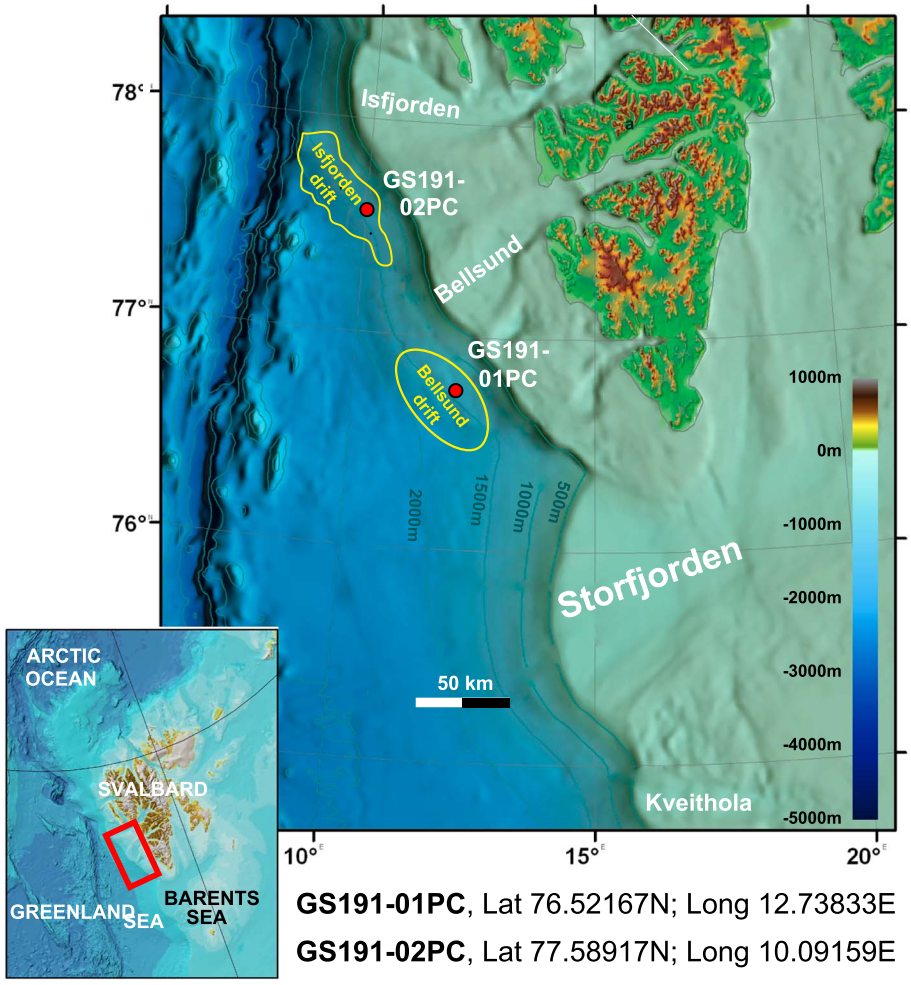

Figure 1. Bathymetric map of the study area with location of the sediment drifts and sediments cores (modified after Rebesco et al., 2013).

northward moving Norwegian Deep Sea Water, receiving periodic, across-slope, sediment inputs through sediment laden, dense shelf waters masses. Dense, cold, and saline water masses form on the shelf during winter by persistent freezing and brine rejection in polynyas of the Barents Sea. These dense water masses incorporate sediments by basal erosion while they move toward the shelf break and cascade along the continental slope. The sedimentary sequences recovered from the Bellsund and Isfjorden sediment drifts contain a high-resolution depositional record associated with past climate changes that can contribute significantly to the reconstruction of the Svalbard-Barents Sea ice sheet history and related palaeoceanographic configuration.

3. Material and Methods

Two Calypso giant piston cores were collected at the crest of the Bellsund (GS191-01PC—1,647-m water depth) and Isfjorden (GS191-02PC—1,322-m water depth) sediment drifts during the Eurofleets-2 PREPARED cruise, on board the R/V G.O. Sars (Lucchi et al., 2014; Figure 2).

The sediment cores were X-radiographed and split in half sections. The archive sections were visually described and photographed with an Avaatech XRF core scan digital camera.

A total of 26 samples (15 samples from core GS191-01PC and 11 samples from core GS191-02PC) were collected for AMS (accelerator mass spectrometry) radiocarbon (^{14}C) dating performed at NOSAM Laboratory (United States) on monospecies samples of N. *pachyderma* (*sin*) or on mixed planktonic foraminiferal tests.

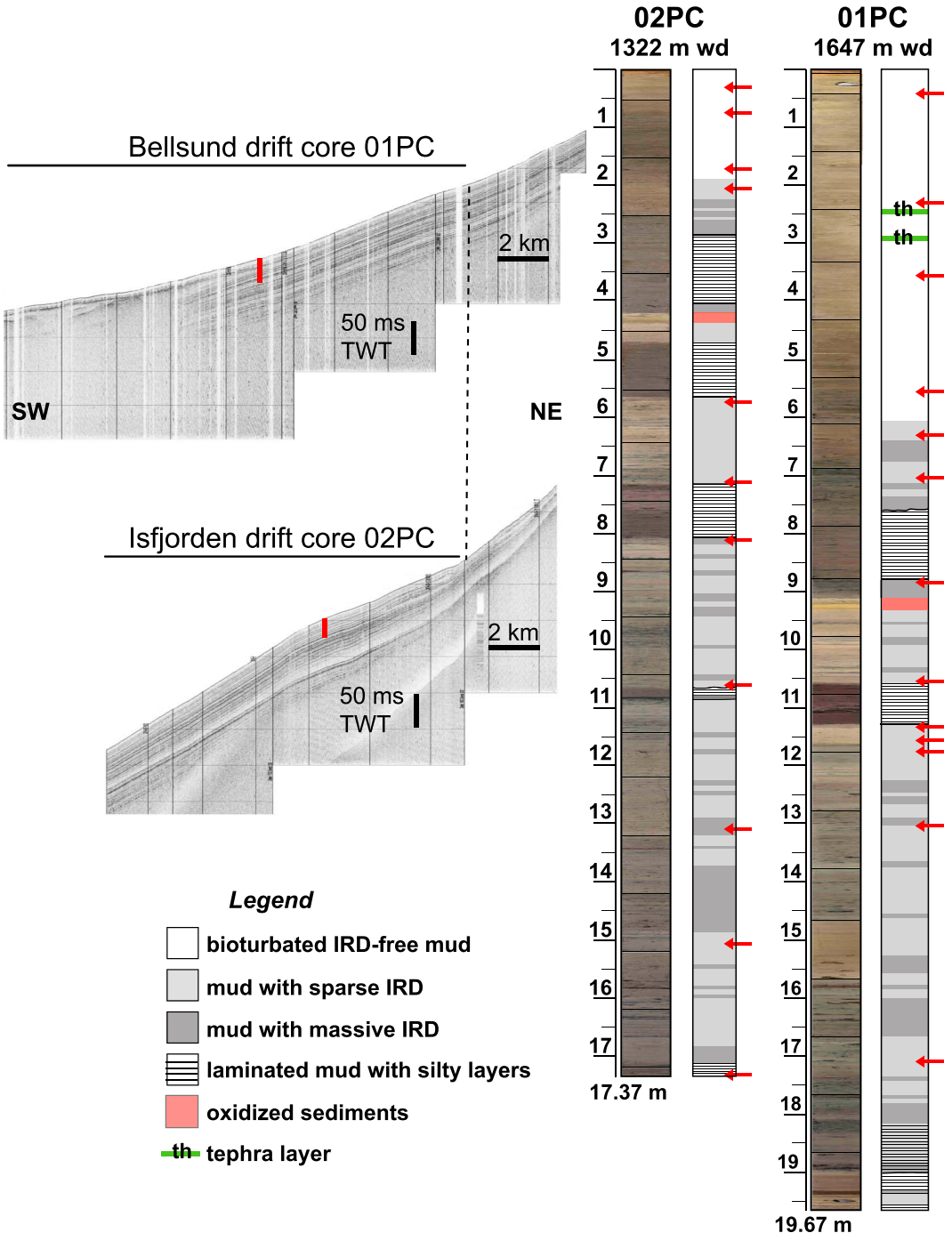

Figure 2. Downslope oriented subbottom profiles indicating the location of the studied Calypso cores (red segments). The dashed line indicates the upslope limit of the plastered contourite drifts and visualizes the depositional architecture of the slope. On the right side are the detailed photographs and lithologic logs of the two long cores GS191-01PC (1,647-m water depth) and GS191-02PC (1,322-m water depth). Red arrows indicate the location of the radiocarbon dated horizons. See legend for lithological details.

The raw ^{14}C data were calibrated with the CALIB software version 7.1 (Stuiver & Reimer, 1993) using the Marine13 calibration curve (Reimer, 2013) and applying a global ocean reservoir correction (R) of 400 years and an average marine regional reservoir effect $\Delta R = 105 \pm 24$ to accommodate local effects, on the Svalbard area as indicated by Mangerud et al. (2006) and Bondevik et al. (2006). We kept the same calibration over the entire core length, although we are aware that the values of the reservoir correction should vary throughout

Table 1
Accelerator Mass Spectrometry ^{14}C Dating

Laboratory ID	Sample ID (-cm bsf)	^{14}C year BP	^{14}C year BP error	Calibrated year BP 1σ	Calibrated year BP 2σ	Calibrated year BP median probability
OS-123414	GS191-01PC-45	1740	40	1166–1271	1074–1305	1212
OS-123438	GS191-01PC-231	4850	30	4912–5087/5093–5114	4859–5209	5017
OS-130680	GS191-01PC-360	7330	20	7673–7755	7645–7805	7718
OS-130677	GS191-01PC-552	8560	45	9019–9174	8987–9256	9109
OS-130676	GS191-01PC-627	10850	55	12098–12382	12010–12494	12245
OS-130681	GS191-01PC-703	12400	35	13733–13870	13660–13947	13804
OS-130682	GS191-01PC-888	12850	30	14212–14527	14149–14706	14396
OS-123440	GS191-01PC-915	15150	55	17758–17944	17636–18027	17841
OS-123412	GS191-01PC-934	15900	150	18516–18827	18322–18967	18666
OS-123527	GS191-01PC-1053	20200	100	23587–23888	23436–24032	23736
OS-130684	GS191-01PC-1133	20600	70	24073–24306	23957–24418	24190
OS-130685	GS191-01PC-1153	23000	95	26667–27034	26509–27173	26848
OS-130686	GS191-01PC-1172	24400	110	27809–28073	27714–28262	27955
OS-137085	GS191-01PC-1303	31100	420	34615–35440	34218–35886	35027
OS-123407	GS191-01PC-1713	34900	1500	36966–40388	35522–41726	38722
OS-123787	GS191-02PC-26	3340	25	3032–3173	2955–3233	3102
OS-123531	GS191-02PC-75	8210	35	8539–8694	8462–8802/8825–8837	8621
OS-123792	GS191-02PC-172	9970	60	10741–10974	10664–11081	10863
OS-123415	GS191-02PC-202	10950	110	12212–12565	12005–12636	12361
OS-123532	GS191-02PC-567	16850	80	19629–19894	19537–20020	19770
OS-123533	GS191-02PC-708	19950	110	23283–23650	23078–23800	23463
OS-123534	GS191-02PC-824	21200	120	24762–25222	24525–25344	24980
OS-123403	GS191-02PC-1064	33100	990	35662–38027	34651–38983	36799
OS-123535	GS191-02PC-1306	42800	1700	44110–47329	42897–49069	45775
OS-123802	GS191-02PC-1506	44500	4800	44304–50000	39240–50000	45934
OS-123801	GS191-02PC-1733	>48600				>50000

Note. Sample ID report indication of sample depth.

time, particularly in relation to climatic changes that are responsible for pronounced modifications of sea water temperature, chemistry, and vertical mixing, affecting the reservoir capability. The calibrated ages in calendar year are provided with their $\pm1\sigma$ and $\pm2\sigma$ ranges and indicated as cal year BP and cal kyr BP (Table 1). The median of the calibrated probability distribution is used in this work since this value is considered the most probable approximation to a real calendar age (Telford et al., 2004).

A total of 72 sediment samples have been collected from core GS191-01PC and analyzed to determine the presence of volcanic glasses and/or tephra layers. Of those, 60 samples have been collected every 10 cm between 0 and 6 m below sea floor (mbsf), and additional 12 samples have been collected from significant peaks of the magnetic susceptibility down core profile along the whole core length. The samples were studied under the stereomicroscope to assess the different components in a qualitative way and to screen the possible presence of volcanic ash layers. The samples containing volcanic ash particles were mounted in epoxy resin and prepared as standard polished thin sections for textural and geochemical measurements. Relative abundance of volcanic particles and their texture were measured using a scanning electron microscope using a Zeiss EVO MA. Major and minor element geochemical analysis of volcanic glass shards were carried out by a JEOL JXA 8200 electron microprobe equipped with five wavelength-dispersive spectrometers. A beam accelerating voltage of 15 kV was used with a beam current 15 nA, probe diameter 10 μm, with acquisition time 10 and 5 s for peak and background, respectively. The instrument was calibrated using appropriate mineral standards. Analytical errors were estimated from mineral and natural glass standards and are typically <1% for major elements (>1 wt.%), and <5% for minor elements (0.1–1 wt.%).

The working sections of the sediment cores were subsampled with u-channel plastic holders for continuous paleomagnetic and rock magnetic analyses including (i) natural remanent magnetization (NRM) measured on a small-access (45-mm diameter) automated pass-through "2G Enterprises" DC 755 superconducting rock magnetometer (SRM); and (ii) low-field magnetic susceptibility (k), measured using a Bartington magnetic susceptibility meter equipped with probe MS2C and mounted in-line with the SRM translating system.

After magnetic susceptibility measurements, the NRM was subjected to alternating field (AF) demagnetization steps up to a maximum peak field of 100 mT (steps: 0, 5, 10, 15, 20, 30, 40, 50, 60, 80, and 100 mT). Afterward anhysteretic remanent magnetization (ARM) was imparted on each u-channel, using an in-line single axis direct current (DC) coil, coupled with the AF coils. While the u-channel was translated through the AF and DC coil system at a constant speed of 10 cm/s, an axial 0.1 mT bias DC field and a symmetric AF peak of 100 mT along the Z axis were applied. The k and ARM intensities depend on ferromagnetic minerals concentration. The k values are controlled by the contribution of all the rock-forming minerals, while the ARM is related to the concentration of fine, single-domain (SD), ferrimagnetic grains (Maher, 1988). The median destructive field (MDF), which is the value of peak AF required to reduce the remanence intensity to half of its initial value, was computed from AF demagnetization curves (MDF_{NRM} and MDF_{ARM}). Since high values of ARM/k ratio suggested the presence of SD grains, while low values indicate the multidomains grains (Banerjee et al., 1981), ARM/k parameter was used to estimate ferrimagnetic grain size trends. ΔGRM/ΔNRM was computed by means of DAIE software (Sagnotti, 2013) in order to have a proxy for the occurrence of iron sulfides (Fu et al., 2008) and to quantify the tendency to acquire a spurious gyromagnetic remanent magnetization (GRM) at high AF demagnetization steps.

4. Results

4.1. Lithofacies Description

Both cores are dominated by mud, mainly bioturbated and also with intervals of other sedimentary structures such as laminations and massive/diffuse presence of ice rafted debris (IRD). We considered as IRD only the pebble-sized fraction (>2 mm) as it can be associated to iceberg rafting only, since a transport by contour current would require unrealistically high flow velocities. The two studied cores contain the following main lithofacies (Figure 2):

i) IRD-free, bioturbated mud, mainly forming the uppermost part of the cores;
ii) IRD-rich, bioturbated mud. IRD occur with different concentrations: from massive high concentration of pebbles and cobbles defining a layer to sparse with random distribution. The latter sublithofacies is predominant in the lower half of both cores; and
iii) Finely laminated, massive (not bioturbated) mud with silt layers. This facies is confined in discrete intervals several centimeters thick.

A well-defined oxidized muddy interval overlain by massive IRD is present in both cores at 9.1–9.3 and 4.2–4.4 mbsf in core GS191-01PC and GS191-02PC, respectively.

4.2. ^{14}C AMS Dating

The radiocarbon dates indicate that core GS191-01PC contains an expanded sequence with respect to core GS191-02PC: in the former, nearly 20 m of sediment was deposited during about 40 kyr, whereas in the latter, about 17 m of sediments deposited during over 50 kyr (Table 1). The uppermost 5.70 m of the IRD-free, bioturbated mud in core GS191-01PC was deposited in about 10 kyr, whereas the same lithostratigraphic facies in core GS191-02PC is 2.80-m thick only. A comparison made between the sedimentary sequence recovered in the two long piston cores with the respective box cores retrieved from the same sampling sites confirmed the full recovery of the depositional sequences without any sediment loss at the top of the long cores. Therefore, the different thicknesses of the chronostratigraphic intervals have to be solely related to the different sedimentation rate at the two sampled sites

Radiometric dates allowed us to constrain the age of some lithological units and marker beds like the above mentioned red oxidized layer overlain by massive delivery of IRD, which was deposited at around 18 kyr, or the laminated intervals with silty layers, whose bases are dated sequentially at 14.3, 19.7, and 24.2 kyr. Further age constraints, also in combination with paleomagnetic data, will be discussed in section 5.1, which discusses the age model at high resolution.

4.3. Tephra Analysis

Of the overall investigated samples, only seven samples were found to contain rare glass shards (<5 per gram of sediment), and only two samples, located at 2.48 and 2.98 mbsf, were characterized by a distinct shard peak concentration (>30 per gram of sediment) and therefore suitable for geochemical investigation. We

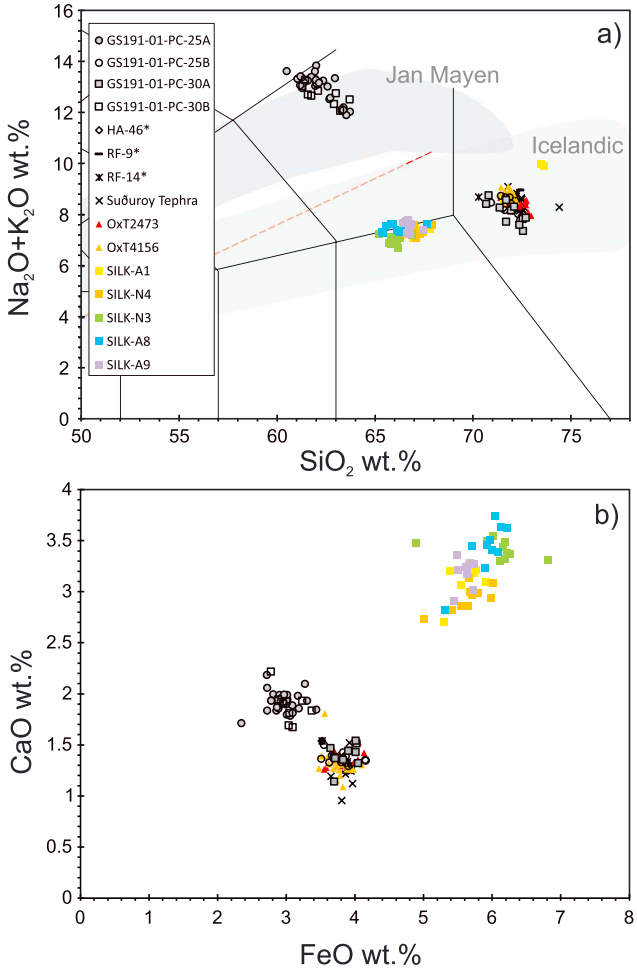

Figure 3. (a) Total alkali versus silica diagram of Le Bas et al. (1986) and (b) CaO versus FeO diagram showing GS191-01PC-25 and GS191-01PC-30 cryptotephra composition compared with Suðuroy tephra (Pilcher et al., 2005; Wastegård, 2002), HA-46*, RF-9*, and RF-14* tephra layers (Óladóttir et al., 2008), OxT2473 and OxT4156 cryptotephra (Housley et al., 2012), and selected Holocene tephra from Katla system (SILK; Larsen et al., 2001). For comparison, the compositional fields of the products erupted by Jan Mayen (Imsland, 1984) and the Iceland (Jennings et al., 2014; Larsen et al., 2001; Óladóttir et al., 2008) are also reported. Red dashed line separates alkaline and subalkaline fields (Irvine & Baragar, 1971).

will refer to those two samples as a cryptotephra: an interval containing particles with size ranging from 30 to 50 μm, consisting of moderately to incipiently vesicular shards with spherical or slightly elongated vesicles, blocky dense glass shards and *y* shaped, thin-walled bubbles junctions.

Cryptotephra from sample GS191-01PC-25 (2.48 mbsf) involves a mixed layer comprised of two distinct chemical compositions. Most of the particles (n = 35; GS191-01PC-25A) have rather homogeneous composition with 60.49–63.50 wt.% SiO_2 and 12.00–13.83 wt.% alkali and plot in the trachyte fields of the total alkali-silica diagram (TAS; Le Bas et al., 1986—Figure 3 and Table 2). It is noteworthy that almost all the glasses with this composition are incipiently altered and characterized by a low total oxide (<95 wt.%). The second glass population (n = 20; GS191-01PC-25B) has a homogenous rhyolitic composition with 70.92–72.65 wt.% SiO_2 and 8.00–8.72 wt.% alkali. Similarly, in sample GS191-01PC-30 (2.98 mbsf) the glass shards present a bimodal chemical composition. Most of the glass particles (n = 19; GS191-01PC-30A) have a homogeneous rhyolitic glass composition with 70.66–72.45 wt.% SiO_2 and 7.33–8.73 wt.% alkali. The second less abundant group of glass shards (n = 18; GS191-01PC-30B) has a trachyte composition with 58.34–63.66 wt.% SiO_2 and 12.64–13.26 wt.% alkali. Also in this case, glasses are characterized by a rather low total oxide (<95 wt.%). Glass compositions of sample GS191-01PC-30 completely match those of sample GS191-01PC-25 (Figure 3 and Table 2).

4.4. Rock Magnetism and Paleomagnetism

Data analyses provided information about variation in the type and concentration of magnetic minerals as well as about stratigraphic trends of paleomagnetic inclination, declination, and relative paleointensity.

A well-defined characteristic remanent magnetization (ChRM) was isolated and its direction was computed by principal component analysis with the DAIE software (Sagnotti, 2013). After removal of the viscous low-coercivity remanence component (at AF peaks of 0–10 mT), all the stratigraphic sections display a normal polarity single-component remanence, with the exception of the last u-channel of Core GS191-01PC, where two opposite remanence components (normal and reverse) have been observed.

In both core GS191-01PC and core GS191-02PC the ChRM was isolated for the 10- to 60- and 10- to 80-mT demagnetization steps (Figures 4a–4c and 4g–4l). In the lowest u-channel of core GS191-01PC, after removal of the viscous overprint, a normal component is removed between 10 and 30 mT and a reverse component is then isolated and removed between 30 and 80 mT (Figures 4d–4f).

As the cores were not azimuthally oriented, the ChRM declination of each u-channel was arbitrarily oriented in order to line up the average declination values for each u-channel to geographic north. Therefore, the mean declination value of each u-channel was considered as rotation angle and had been subtracted (or added) to each measured declination value. In any case, paleomagnetic declinations are poorly defined since paleomagnetic vectors are very steep at the high latitude of the core sites and they were not taken into account for core correlation.

In core GS191-01PC, the k stratigraphic trend is characterized by a large peak at the bottom (~19 mbsf), reaching the maximum value of 445×10^{-5} SI (Figure 5). For the remaining part of the core, k values show limited oscillation around a mean value of 53.4×10^{-5} SI with the exception of two intervals, around 11 mbsf (IRD rich level—green rectangle) and 8 mbsf (interlaminated facies—yellow rectangle) where lowest values were measured. The ARM displays the same trend as k, with a distinct increase from 7.5 mbsf toward the top

Geochemistry, Geophysics, Geosystems

10.1029/2018GC007955

Table 2
Tephra Chemical Composition

Sample	ICPO-G S191-25A (2.48 mbsf)		ICPO-G S191-25B (2.48 mbsf)		ICPO-G S191-30A (2.98 mbsf)		ICPO-G S191-30B (2.98 mbsf)		OxT2473		OxT4156		HA-46*		RF-9*	RF-14*		Suðuroy (Wastegård, 2002)		Suðuroy (Pilcher et al., 2005)	
Age	7132 and 7769 years cal. BP								7660–7515 cal. BP		7660–7515 cal. BP		7020 (SAR)		7460 (SAR)	7550 (SAR)				~6050 BC	
	$n = 35$	st. dev	$n = 20$	st. dev	$n = 19$	st. dev	$n = 18$	st. dev	$n = 14$	st. dev	$n = 22$	st. dev	$n = 2$	st. dev		$n = 2$	st. dev	$n = 10$	st. dev	$n = 9$	st. dev
SiO_2	62.23	0.87	71.88	0.44	71.85	0.69	62.33	0.89	72.20	0.51	71.78	0.21	71.26	0.39	71.98	70.98	0.29	72.47	0.71	72.27	0.22
TiO_2	0.40	0.06	0.31	0.08	0.35	0.08	0.39	0.08	0.31	0.05	0.30	0.03	0.75	0.06	0.27	0.35	0.05	0.20	0.04	0.30	0.02
Al_2O_3	19.04	0.52	13.94	0.40	14.04	0.53	19.13	0.73	13.50	0.21	13.58	0.16	13.94	0.06	13.85	13.85	0.08	13.28	0.45	13.83	0.10
FeO	2.95	0.21	3.81	0.21	3.86	0.15	3.04	0.18	3.85	0.17	3.77	0.17	3.51	0.09	3.69	4.23	0.1	3.87	0.10	3.86	0.06
MgO	0.23	0.10	0.11	0.12	0.16	0.13	0.20	0.06	0.14	0.05	0.15	0.05	0.15	0.01	0.15	0.13	0.06	0.15	0.02	0.00	0.00
MnO	0.24	0.07	0.24	0.10	0.21	0.06	0.29	0.13	0.21	0.03	0.20	0.02	0.55	—	0.10	0.21	—	0.18	0.02	0.18	0.02
CaO	1.92	0.10	1.37	0.06	1.40	0.11	1.88	0.16	1.37	0.08	1.31	0.13	1.53	0.02	1.02	1.44	0.02	1.25	0.15	1.32	0.03
Na_2O	5.40	0.30	4.87	0.21	4.63	0.35	5.33	0.60	5.07	0.27	5.25	0.17	4.77	0.18	5.30	5.10	0.19	5.00	0.56	4.60	0.23
K_2O	7.53	0.50	3.43	0.15	3.43	0.16	7.35	0.74	3.35	0.12	3.50	0.09	3.43	—	3.61	3.67	0.12	3.60	0.35	3.65	0.08
P_2O_5	0.06	0.07	0.00	0.10	0.07	0.09	0.06	0.09	—	—	0.04	0.02	0.12	0.01	0.03	0.05	0.05	—	—	—	—
Total	100.00		100.00		100.00		100.00		100		100.00		100.00		100.00	100.00		100.00	0.27	100.00	0.22
Alkali	12.93	0.56	8.29	0.30	8.06	0.44	12.67	0.36	8.41	0.26	8.75	0.18	8.20	0.18	8.91	8.77	0.31	8.60	0.91	8.25	0.32

Note. HA-46*, RF-9*, and RF14* ages are calculated from the soil accumulation rate (SAR) (before 2005). st.dev = standard deviation.

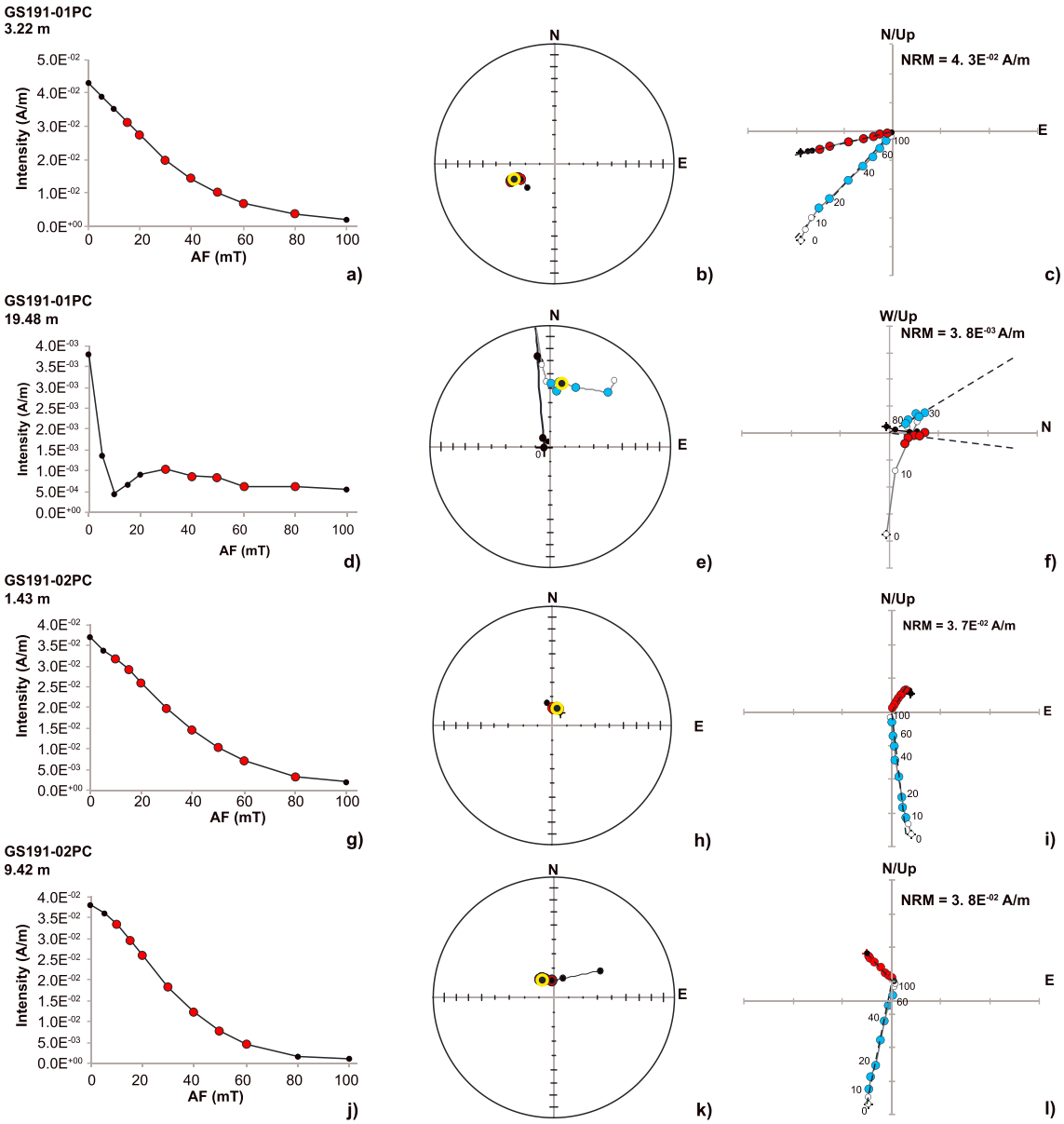

Figure 4. Representative natural remanent magnetization (NRM) demagnetization graphs for selected specimens subjected to alternating field (AF) demagnetization. The demagnetization data have been visualized and analyzed using the DAIE program (Sagnotti, 2013). From top to bottom: (a, d, g, and j) variations of the NRM intensity as a function of the demagnetization steps; (b, e, h, and k) stereographic (equal area) projection of unit vectors defined at each demagnetization steps, (c, i, l, and f) Orthogonal projection diagrams of vector measured at each demagnetization step with projection on the N-S vertical plane, and (f) W-E vertical plane. Black (white) circles indicate projection on the lower (upper) hemisphere. The red symbols (for the lower hemisphere projection) and light blue (for the upper hemisphere projections) indicate the demagnetization steps selected for the principal component analysis (PCA). NRM direction is marked by a cross superimposed on the circle. In the stereographic projection the black-yellow circle indicates the computed characteristic remanence component.

highlighting an increase in the concentration of ferrimagnetic minerals (Figure 5). Also, the ARM/*k* parameter shows two minima in correspondence of IRD-rich level and interlaminated facies and an increase from about 7.5 mbsf upward suggesting an increase in fine-grained ferrimagnetic minerals. The MDF_{NRM} displays little fluctuation around a mean value of about 30 mT, with few exceptions. In particular, minimum MDF_{NRM} values of about 5 mT were measured at about 19.5 and 11 mbsf (indicated blue arrows in Figure 5). The latter minimum occurs within a stratigraphic interval of interlaminated facies, at the top of an interval between 12.5 and 10.5 mbsf characterized by variations of large amplitude. A maximum peak up to ~50 mT was observed at ~19 mbsf in correspondence of IRD rich layer (red

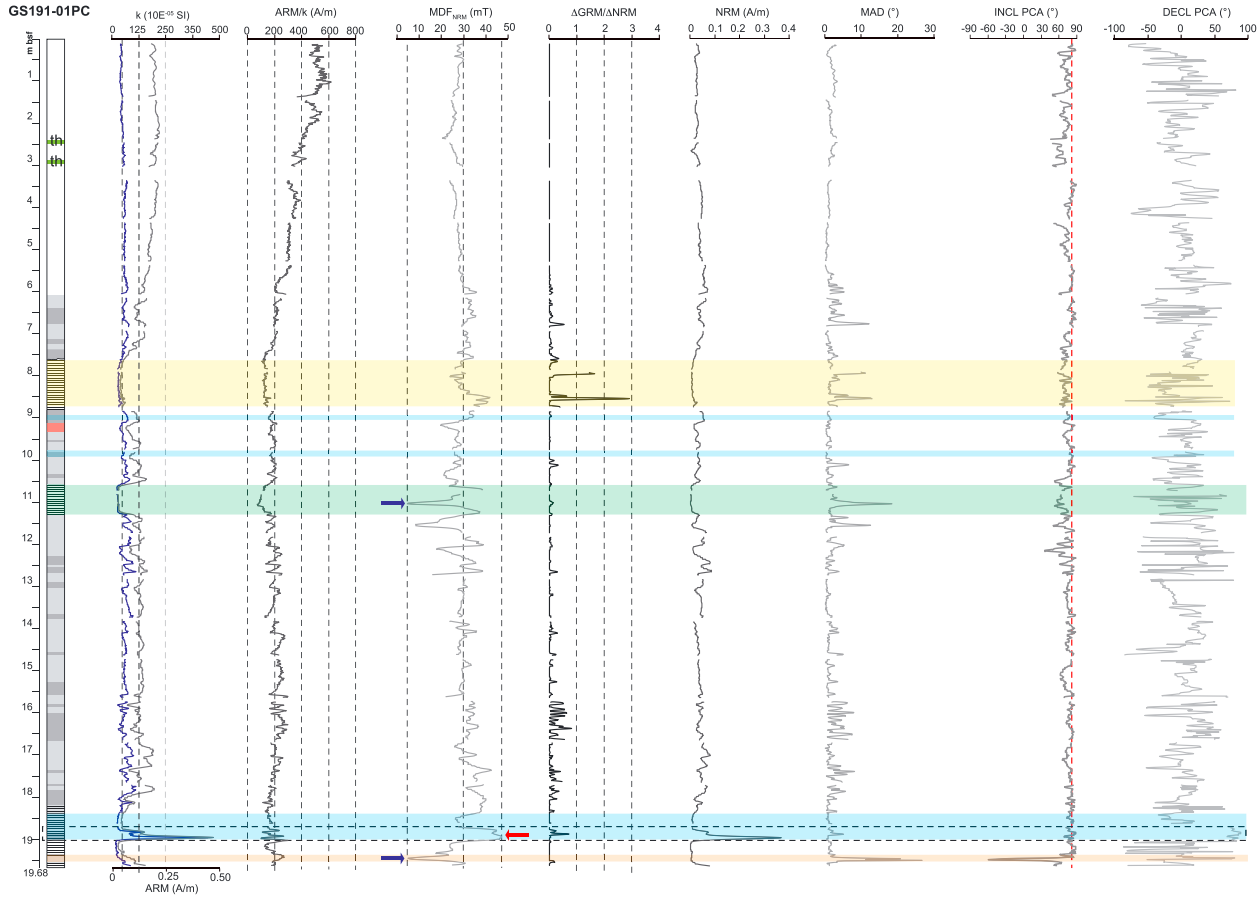

Figure 5. Along core variation of the main rock magnetic and paleomagnetic parameters measured for the core GS191-01PC. The plots show the stratigraphic trend of the intensity of ARM (gray line), the magnetic susceptibility *k* (blue line), the ARM/*k* ratio, the MDF_{NRM}, ΔGRM/ΔNRM ratio, natural remanent magnetization (NRM), the maximum angular deviation (MAD), ChRM inclination, and ChRM declination. Blue arrows point out two minimum values of the MDF_{NRM} parameters (around 5 mT) at ~19.5 and 11 mbsf. Red arrow indicates the maximum peaks of MDF_{NRM} (up to 50 mT) at ~19 mbsf in correspondence of an IRD rich layer. The vertical red dashed line in the inclination plot indicates the value expected at the core site for a geocentric axial dipole field. The orange band indicates the interval correlated to the Laschamps excursion. ARM = anhysteretic remanent magnetization; MDF = median destructive field; GRM = gyromagnetic remanent magnetization; ChRM = characteristic remanent magnetization; IRD = ice rafted debris; INCL = inclination; DECL = declination.

arrows in Figure 5) and high values MDF_{NRM} of about 40–45 mT were measured between 18.5 and 17.3 mbsf, as well as at the onset of interlaminated layer around 8.6 mbsf.

The MDF_{NRM} measured in the lowest u-channel of core GS191-01PC is affected by the presence of two antipodal remanence components, as discussed above, and it is therefore not indicative of a change in the composition of the magnetic carriers. Overall, the MDF_{NRM} trend, with values in the range typical for pseudo SD to SD magnetite (Maher, 1988), indicates that low-coercivity ferrimagnetic grains are the main magnetic carriers.

The acquisition of spurious GRM at high AF steps is absent for a large part of the core; only two narrow peaks (with values of 2.9 and 1.6) were observed in the interlaminated facies around 8 mbsf.

The NRM shows the same trend of ARM and *k* parameters, with a peak at the base of the core (3.68×10^{-1} A/m), and lower values in correspondence of IRD rich layer and interlaminated facies (green and yellow rectangle, Figure 5). However, no distinct increase was measured for NRM values in the interval from 7.5-mbsf depth upward.

The maximum angular deviation (MAD) was computed for each determined ChRM direction (Figure 5). The MAD is generally lower than 10°, with some few exceptions that correspond to (i) interlaminated layer (12°), (ii) layer rich in IRD (18°), and (iii) lower portion of the core (19.49 mbsf) where it reaches 25°.

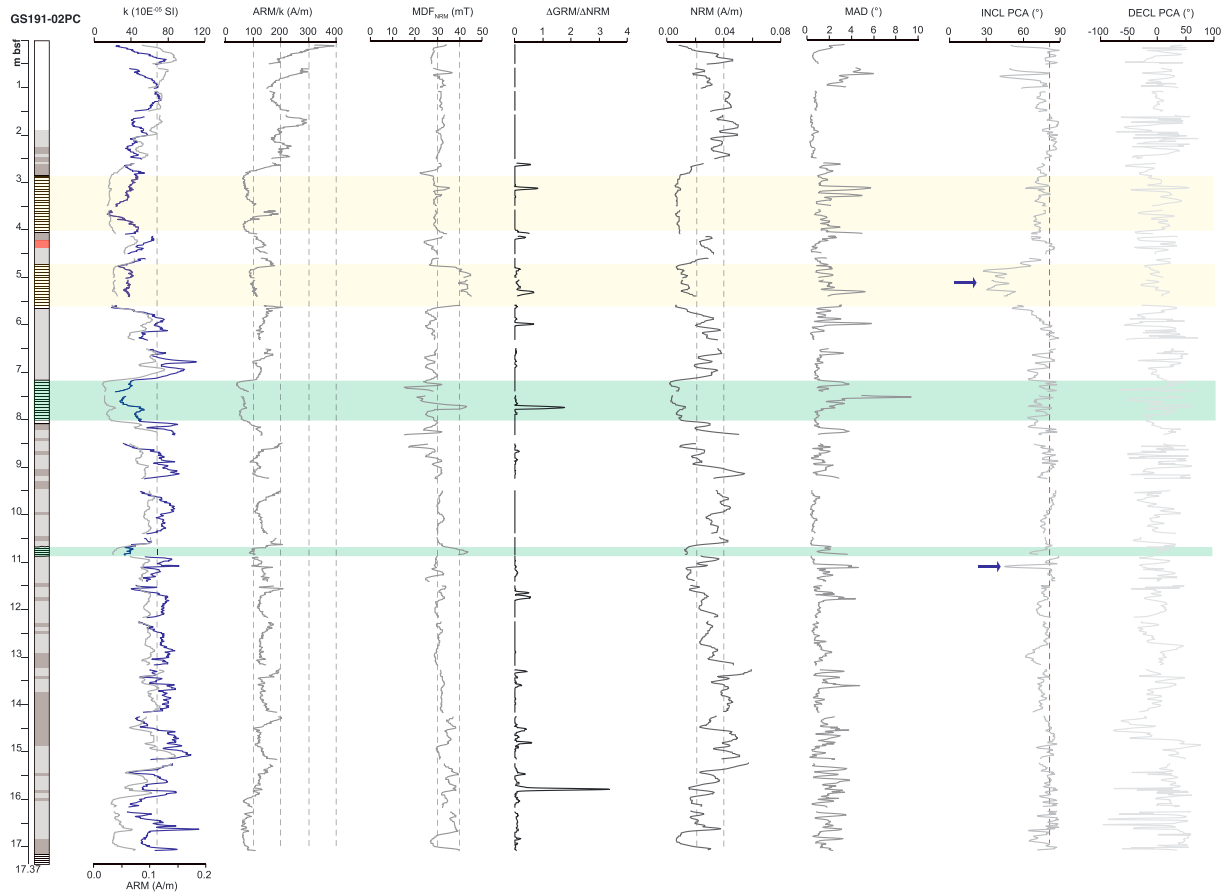

Figure 6. Along-core variation of the main rock magnetic and paleomagnetic parameters measured for the core GS191-02PC. The plots show the stratigraphic trend of the intensity of the ARM (gray line), the magnetic susceptibility k (blue line), the ARM/k ratio, the MDF_{NRM}, ΔGRM/ΔNRM ratio, natural remanent magnetization (NRM), the maximum angular deviation (MAD), ChRM inclination, and ChRM declination. The blue arrow points out intervals of low inclination around ~11 mbsf (inclination decreases down to 40°) and between 5.6 and 4.7 mbsf (inclination decrease down to 30°). The vertical red dashed line in the inclination plot indicates the value expected at the core site for a geocentric axial dipole field. ARM = anhysteretic remanent magnetization; MDF = median destructive field; GRM = gyromagnetic remanent magnetization; ChRM = characteristic remanent magnetization; IRD = ice rafted debris; INCL = inclination; DECL = declination.

The ChRM inclination oscillates around 77° showing a slightly lower value than expected (82.4°, indicated by a red dashed line in Figure 5) for a geomagnetic axial dipole field at 75°N latitude (Figure 5). Moreover, in the lowermost 50 cm low to reverse inclination values have been observed (ChRM inclination reaches −58.6°).

In core GS191-02PC, from Isfjorden sediment drift, the k stratigraphic trend generally oscillates around a mean value of 76×10^{-5} SI. Moving toward the top four intervals of minimum k values have been observed, corresponding to IRD rich levels (~10.8 and 7.5 mbsf—green rectangle) and interlaminated facies (~5.3 and 3.5 mbsf—yellow rectangle). ARM and ARM/k parameters show the same trend of k with low values in correspondence of the same levels (Figure 6). Both the parameters increase from 2.5 mbsf up to the top indicating an increment in the concentration of fine-grained magnetic minerals.

The stratigraphic trend of the MDF_{NRM} parameter displays a slight increase in the same stratigraphic levels where k, ARM, and NRM decrease. In detail, the MDF_{NRM} trend shows limited oscillation around a mean value of 30 mT, with slightly higher values up to 43 mT measured in the interlaminated layers and in the levels rich in IRD. As for core GS191-01PC, the MDF_{NRM} values vary in the range typical for pseudo SD to SD magnetite (Maher, 1988). In core GS191-02PC the acquisition of spurious GRM at high AF steps is almost absent or negligible. Only two narrow peaks of ΔGRM/ΔNRM parameter has been observed at 7.3 mbsf in the IRD layer and at 15.8 mbsf, with values up to 3.36. The NRM intensity oscillates around a mean value of 3.60×10^{-2} A/m with the same trend of k and ARM parameters. The MAD is lower than 10° indicating that the ChRM has been determined with low uncertainty.

The ChRM inclination displays a mean value of 77°, also in this case about 5° lower than that expected for a geomagnetic axial dipole field at 75°N latitude (red dashed line in Figure 6). Moreover, a sharp interval of low inclination has been observed around ~11 mbsf, where the inclination decreases down to 40°, and a wider interval of inclination shallowing (inclination down to 30°) was measured in the interlaminated facies (5.6–4.7 mbsf; blue arrows—Figure 6).

Ferrimagnetic minerals are the main magnetic carries in both cores, with low variation in their concentration, composition and magnetic grain size. Therefore, for the most part they satisfy the selection criteria recommended to evaluate the sediments suitability for relative paleointensity studies. In detail, we computed the RPI curves by normalizing the NRM intensity for an opportune concentration-dependent rock magnetic parameter (k and ARM intensity; see Tauxe, 1993). The NRM after demagnetization at 20 mT (NRM_{20mT}) was normalized by both magnetic susceptibility (k) and the ARM intensity after demagnetization at 20 mT (ARM_{20mT}). Both methods generate the same RPI pattern, indicating a substantial coherency between the two normalization methods (Figure 7).

For core GS191-01PC, we disregarded the portion between 19 and 18.7 mbsf corresponding to the broad peak relative to IRD rich layer (black dashed rectangle in Figure 5) and characterized by distinctly higher coercivity, as also pointed out by the MDF_{NRM} values.

5. Discussion

5.1. Cores Correlation

The along-core variation of rock magnetic and paleomagnetic trends, with the distribution of characteristic lithofacies and the ^{14}C ages, contributed to define high-resolution correlation between the cores (Figure 8). Furthermore, core to core correlation has been computed by means of StratFit software (Sagnotti & Caricchi, 2018). This correlation is based on the match of multiple magnetic parameters trends between GS191-02PC and GS191-01PC cores, where the core GS191-01PC has been identified as the "master core." The correlation process is based on the Excel forecast function and linear regression between subsequent couples of selected tie points.

The tie points pairs have been identified by picking characteristic features in the stratigraphic trends of various magnetic and paleomagnetic parameters, the occurrence of characteristic lithofacies, and the available ^{14}C ages (Table 3). The Excel forecast function is then used to compute values between tie point pairs.

This process results in the estimate of the equivalent depth of the correlated curve (GS191-02PC) into the depth scale of the "master" curve (GS191-01PC).

Following the correlation procedure, the NRM, ARM, and RPI stratigraphic trends of the GS191-02PC and GS191-01PC cores robustly matched, with a close correspondence among peaks and troughs (Figures 8b–8d).

5.2. Reconstruction of the Age Model and Stratigraphic Sequence

Taking into account the constraints provided by the calibrated radiocarbon ages and the litostratigraphic information, we compared paleomagnetic records for the PREPARED cores with RPI and inclination variations expected at the core sites according to global geomagnetic field models (SHA.DIF.14k of Pavón-Carrasco et al., 2014; GGF100k of Panovska et al., 2018) and paleointensity stack (GLOPIS-75 of Laj et al., 2004; Figure 9). Correlation between GS191-02PC and GS191-01PC paleomagnetic trends and target curves was accomplished by the StratFit software (Sagnotti & Caricchi, 2018), transferring records to a common age scale using the same method and software employed for between-cores correlation (as described in section 5.1).

Apart for the youngest interval (Holocene), the RPI trend obtained for core GS191-01PC and core GS191-02PC generally follows closely that of the reference "target" curves (Figure 9).

The poor correlation found for the RPI trends of both cores and target curves during Holocene is probably related to the higher ARM values measured for the Holocene parts of the cores with respect to the older intervals (Figures 5 and 6). In fact, the downcore trends of the ARM and ARM/k parameters indicate a significant decrease in the concentration of fine-grained ferrimagnetic minerals in the Holocene interval, especially for core 01PC, which is an indication of diagenetic dissolution. When RPI stratigraphic trends are

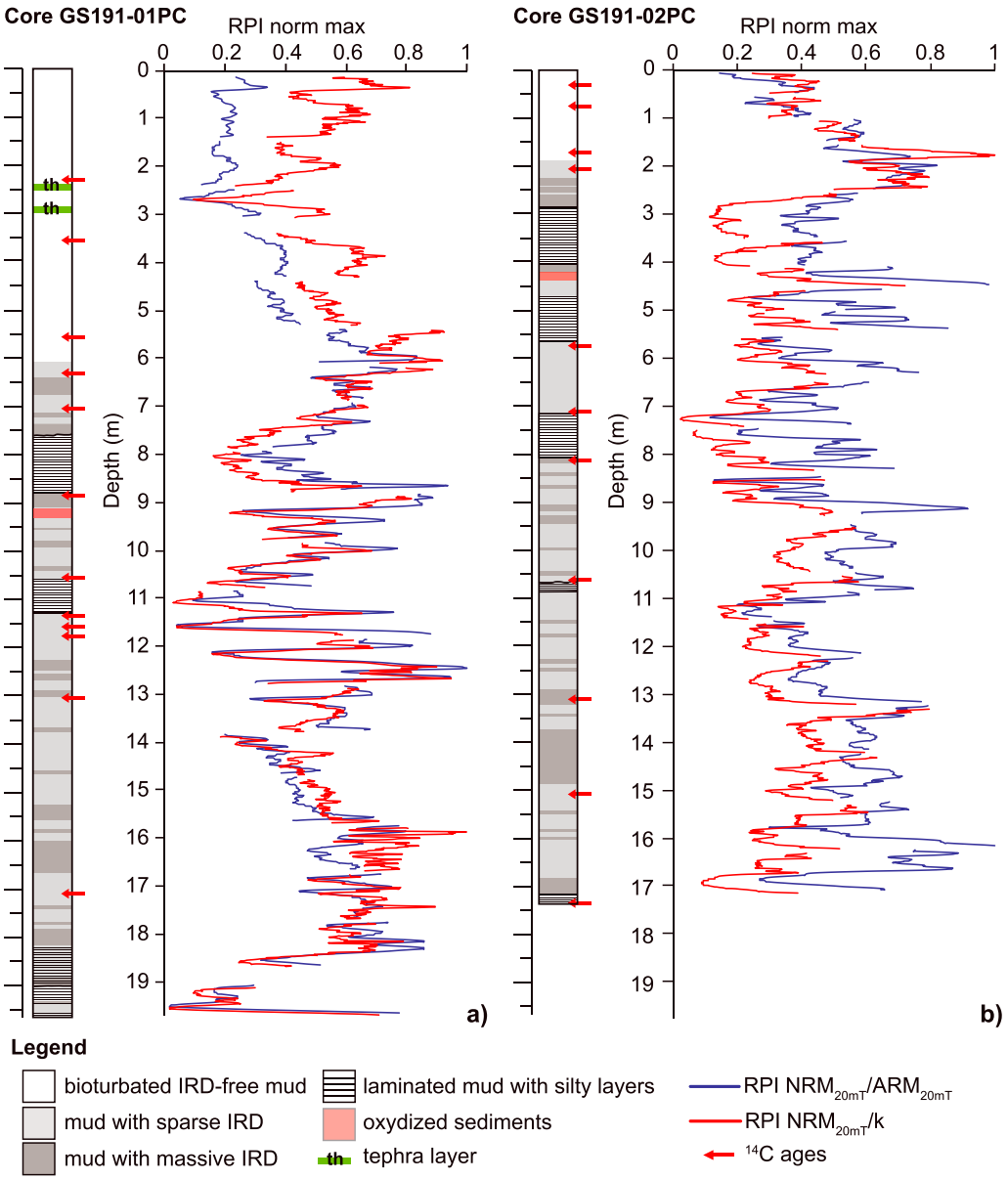

Figure 7. Along core normalized relative paleointensity (RPI) curves NRM_{20mT}/k (red line) and NRM_{20mT}/ARM_{20mT} (blue line) of the analyzed cores (a) core GS191-01PC and (b) core GS191-02PC. IRD = ice rafted debris; NRM = natural remanent magnetization; ARM = anhysteretic remanent magnetization.

computed by scaling the NRM/ARM values to the maximum measured for the whole core, this may result in the observed lower NRM/ARM values in the Holocene interval.

For the rest of the cores the correlation between the PREPARED RPI curves and the trends predicted according to the global geomagnetic field model GGF100k (Panovska et al., 2018) and the paleointensity stack GLOPIS-75 (Laj et al., 2004) is robust, with a close match among peaks and troughs (Figure 9).

These results show that the analyzed successions deposited during a time interval spanning from Holocene to the marine isotopic stage 3 (MIS-3).

According to the paleomagnetic age model, core GS191-01PC contains an expanded stratigraphic sequence with over 6 m of Holocene sediments (0.52 mm/year) and an overall average sedimentation rate of 0.46 mm/year, whereas core GS191-02PC contains a more condensed sequence (the Holocene interval is only 2-m

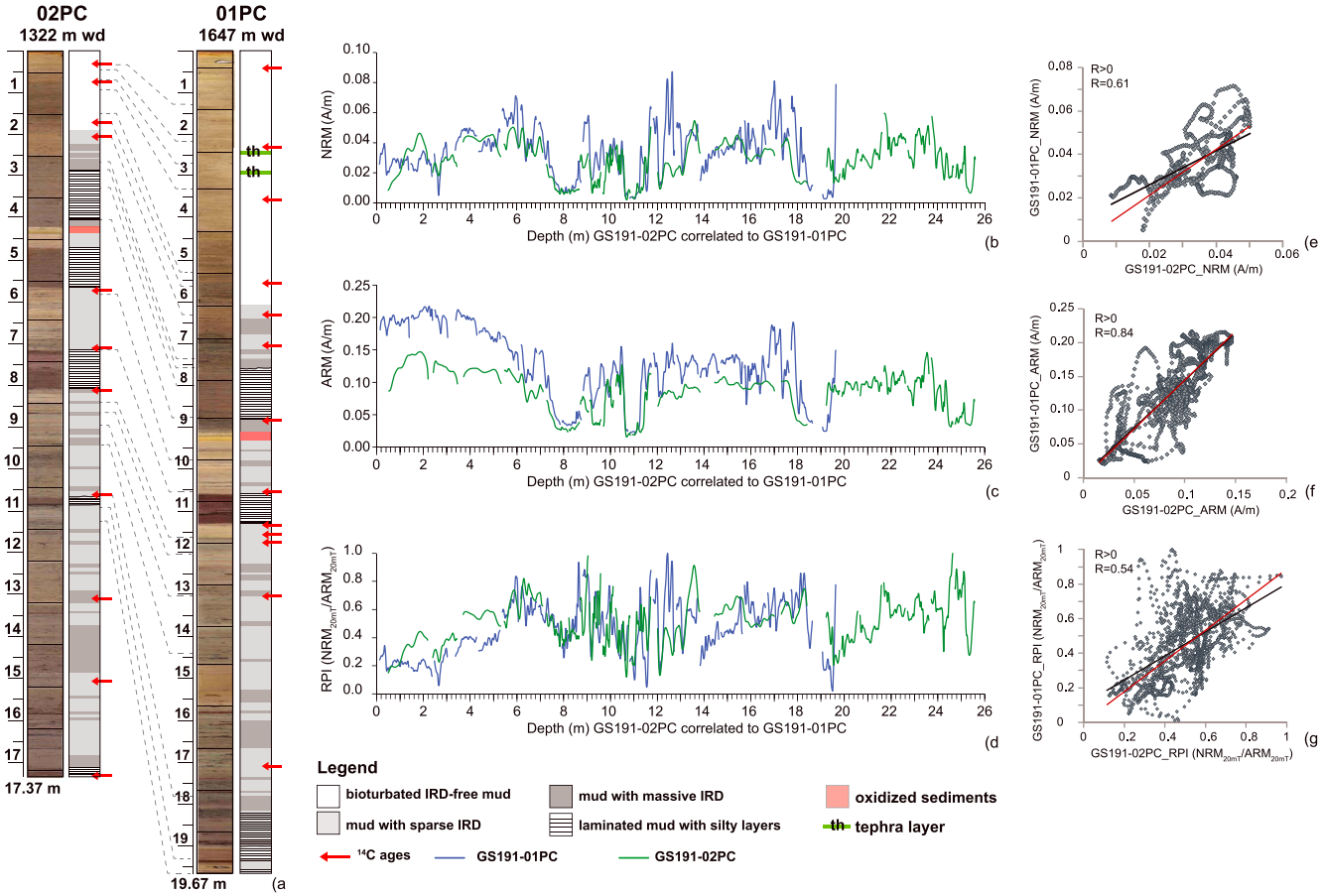

Figure 8. (a) Cores correlation stratigraphy, the red arrows indicate the ^{14}C ages, and the gray dashed line indicate correlation between the adopted tie points; (b) natural remanent magnetization (NRM); (c) anhysteretic remanent magnetization (ARM); and (d) relative paleointensity (RPI) curves. In the correlation procedure (Sagnotti & Caricchi, 2018), all data of core GS191-02PC (green) have been transferred to the stratigraphic depth of GS191-01PC (blue). Following the correlation procedure, the (e) NRM, (b) ARM, and (c) RPI curves of the two cores match with a correlation coefficient $R = 0.61$, $R = 0.84$, and $R = 0.54$, respectively.

thick) spanning down to 60 kyr BP with an overall average sedimentation rate of 0.29 mm/year, nearly half the rate of GS191-02PC.

Moreover, the following stratigraphic intervals were defined in the studied cores and will be discussed in more detail below: the Holocene; the deglaciation phase after last glacial maximum (LGM; MIS-1), the Late Weichselian glacial stage (MIS-2), and the Middle Weichselian interglacial stage (MIS-3). Core GS191-02PC contains also at its base the late termination of the Middle Weichselian glacial stage MIS-4 (between 17 and 17.37 mbsf, dated to 57–60 kyr BP).

5.2.1. Holocene (11.7 cal kyr BP to Present)

The deposition during the Holocene is characterized by IRD-free, bioturbated mud with abundant microfossils indicating environmental conditions favorable to the biological activity. Only the base of the sequence in core GS191-01PC (6.20–5.60 mbsf, corresponding to 11.9–10.6 cal kyr BP) contains some sparse IRD. Two cryptotephra were identified in core GS191-01PC, at the depth of 2.48 and 2.98 mbsf, bimodal by trachytic and rhyolitic volcanic glasses. According to the age model for the GS191-01PC core these layers have an age of 5.2 and 6.3 cal kyr BP, respectively.

The composition of the trachytic glass fully matches that of evolved alkalic products erupted by the Jan Mayen volcano (Imsland, 1984; Figure 3). In particular, the glass compositions are very similar to the Holocene tephras MOR-T2, MOR-T7, MOR-T8, and MOR-T9, reported from lacustrine cores taken from An Loch Mör, Inis Oirr, Aran Islands, and western Ireland (Chambers et al., 2004), all of them attributed to the Jan Mayen volcanic source. Nevertheless, the mentioned reference tephra layers have very recent

Table 3
Tie Points Pairs

GS191-02PC	GS191-01PC
Depth (m)	Depth (m)
0.26	1.30
0.46	2.15
0.68	2.65
0.98	3.43
1.47	5.30
1.72	5.67
2.02	6.36
2.70	7.47
2.80	7.60
3.22	8.00
3.66	8.27
4.11	8.70
4.39	8.99
4.72	9.19
5.85	9.85
7.12	10.58
8.24	11.62
8.55	12.11
8.93	13.09
9.49	14.45
10.00	15.81
10.65	17.80
10.83	18.40
10.88	19.23
11.09	19.50
11.20	19.60
17.50	26.00

ages of 550 cal year BP (MOR-T2) and between 1670 and 1915 cal year BP (MOR-T7-T9), which do not fit with the reconstructed age model. No eruption or tephra layer is reported originating from the Jan Mayen volcano in the time range indicated for the two cryptotephra layers by the age model of the GS191-01PC core. Therefore, the identified cryptotephra layers may be the first evidence of a middle Holocene Atlantic explosive activity from this volcanic source.

Furthermore, the composition of the rhyolitic glass clearly lies into the field of Icelandic volcanic province (Jennings et al., 2014, and references therein; Figure 3), matching the major element composition of evolved silicic products erupted from the Katla volcano (Larsen et al., 2001; Óladóttir et al., 2008). In the middle Holocene the eruption frequency of the Katla volcano was quite high with at least four identified eruptions (Larsen et al., 2001). Chemical composition and time constraint suggest a possible correlation of the cryptotephra sample ICPO-GS191-30 (2.98 mbsf) with the Suðuroy tephra, identified at the Faroe (Wastegård, 2002) and Lofoten Islands that dates ~8000 cal year BP (Pilcher et al., 2005). Good chemical affinity exists also with RF-9* and RF-14* tephra layers identified in on-land soil sections from Iceland and dated respectively 7460 cal year BP and 7550 cal year BP through soil accumulation rate method (Óladóttir et al., 2008), and with the cryptotephra OxT2473 and OxT4156 identified in the open-air archeological site of Ahrenshöft LA 58 D, located in the North Germany (Housley et al., 2012; Figure 3). The latter was dated between 7660 and 7515 cal year BP, and it was correlated to the rhyolitic portion of the Vedde Ash (Younger Dryas), tephra AF555 (late Younger Dryas), and the Suduroy tephra (Preboreal/Boreal) that are indistinguishable from one another. Vice versa, no direct correlation exists between rhyolitic ash population in ICPO-GS191-25 and any known eruption in that time interval. Thus, we infer that this ash peak could be related to reworking of the lowermost tephra, although we cannot exclude that the rhyolitic shards of sample ICPO-GS191-25 can derive from a hitherto unrecognized eruption from Katla volcano.

5.2.2. Deglaciation Phase After LGM (20–12 cal kyr BP)

The sedimentation during this interval is characterized by a variable input of IRD that locally occur massively in association with the progressive decay of the last glacial Svalbard-Barents Sea ice sheet. The stratigraphic record is characterized by the presence of two distinct intervals of interlaminated sediments that were related to intense meltwater release following the lithofacies analysis made by Lucchi et al. (2013).

The younger interlaminated interval, located between 8.8 and 7.6 mbsf in core GS191-01PC and between 4.0 and 2.8 mbsf in core GS191-02PC, is characterized by evident decreases of *k*, ARM and NRM paleomagnetic parameters. These variations could be related to the componentry of the interlaminated interval, mainly made of quartz (diamagnetic mineral) with a minor percentage of rock fragments. Low *k* values can be also linked to the high organic matter content (cf. Lucchi et al., 2013).

Radiocarbon ages on core GS191-01PC indicate deposition occurred during the Bølling warm interstadial. This interlaminated interval was previously identified in many other cores along this margin (Carbonara et al., 2016; Caricchi et al., 2018; Lucchi et al., 2013; Sagnotti et al., 2016) and pointed to represent the Arctic marine record of the Meltwater Pulse-1a (MWP-1a), dated at about 14.6–14.2 kyr BP (Lucchi et al., 2013, 2015).

Another older interlaminated interval was observed in core GS191-02PC between 5.6 and 4.7 mbsf having a basal calibrated radiocarbon age of 19.8 cal kyr BP. As for the younger interlaminated facies, this interval is characterized by a distinct ChRM inclination shallowing, with a clear decrease of *k*, ARM, ARM/*k*, and NRM paleomagnetic parameters. We infer that this interval may correspond to the MWP-19ky, representing the oldest recognized meltwater event occurred after the LGM at around 19 kyr BP (Clark et al., 2004). The apparent shallowing of the inclination observed in this interval does not represent a true geomagnetic

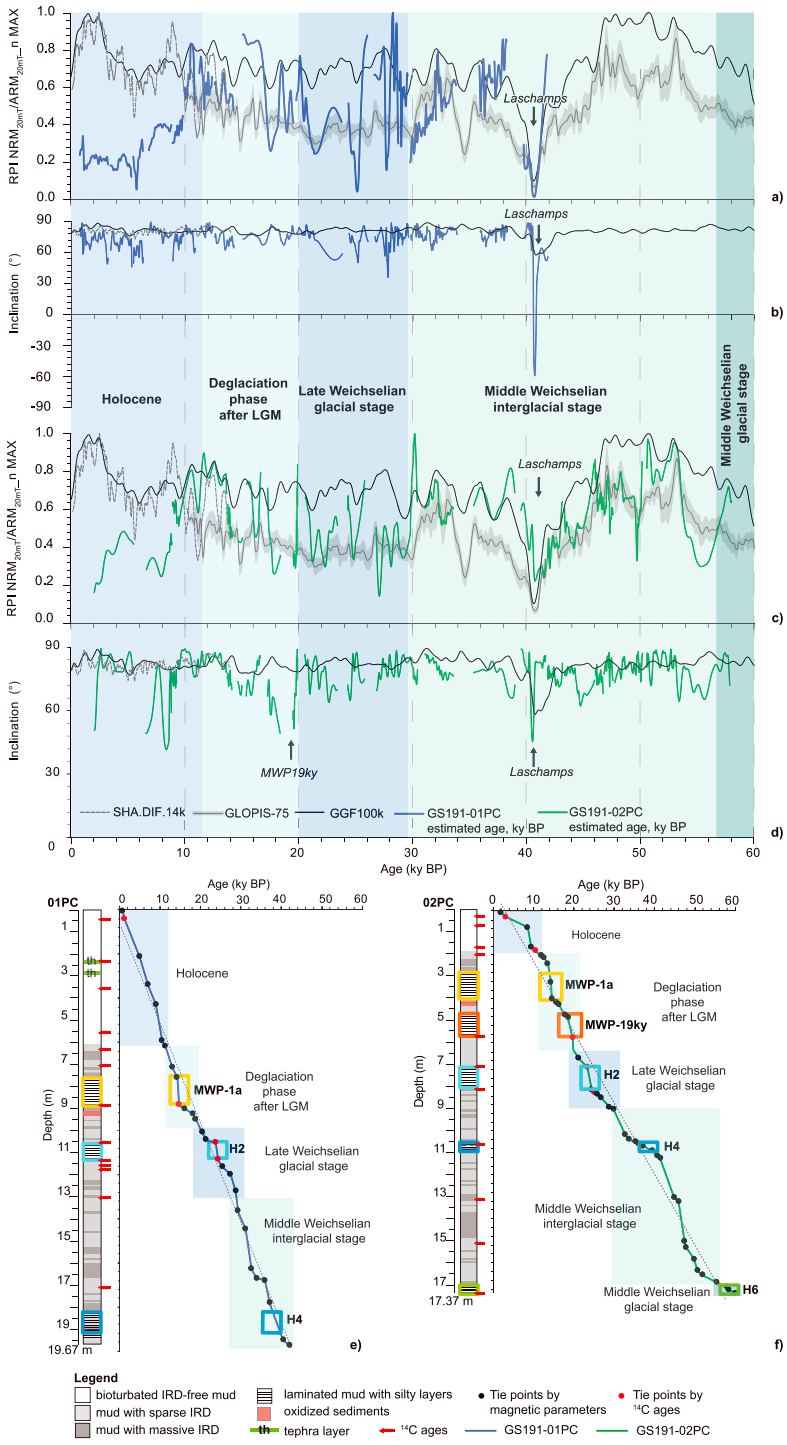

Figure 9. Relative paleointensity of the GS191-01PC (a) and GS191-02PC (c) cores plotted as a function of age and compared with predicted curves from SHA.DIF.14k (Pavón-Carrasco et al., 2014), GLOPIS-75 (Laj et al., 2004), and GGF100k (Panovska et al., 2018) models. Inclination of the GS191-01PC (b) and GS191-02PC (d) cores plotted as a function of age and compared with the inclination trend from the SHA.DIF.14k and GGF100k models. Age model for Core GS191-01PC (e) and GS191-02PC (f). Sedimentation rate drastically increases during the Melt water pulse and Heinrich events (indicated by squares). Red dots indicate accelerator mass spectrometry ^{14}C ages, while black dots indicate the tie-points identified by paleomagnetic and rock magnetic parameters correlations. The dashed lines indicate the linear regression of the age model. Colored band indicate the different stratigraphic intervals. NRM = natural remanent magnetization; ARM = anhysteretic remanent magnetization; RPI = relative paleointensity; IRD= ice rafted debris; LGM = last glacial maximum.

field behavior but rather it is a lithological effect associated to the close interbedding of the finely laminated mud and silt layers, deposited with a different sedimentation rate. The lack of the MWP-19ky in core GS191-01PC, located on the Bellsund drift, may indicate that this area was not affected from this initial melting phase possibly in relation to the shallower bathymetry and smaller size of the Bellsund glacigenic system with respect to the Isfjorden one, making the former less sensitive to the renewed influx of warm West Spitsbergen Current.

According to the age model, the IRD layer located just above the oxidized layer recognized in both cores, has an age of about 16.5 cal kyr BP that matches the timing of the Heinrich event H1 (Hemming, 2004, and reference therein).

5.2.3. Late Weichselian Glacial Stage (29–21 cal kyr BP)

Contrary to the typical glacial sedimentation observed along this margin, which consists of clustered glacigenic debris flows (Vorren & Laberg, 1997), the sampled stratigraphic sequences on the Bellsund and Isfjorden sediment drifts do not contain glacigenic debris flows and the glacial stage at both sites is rather characterized by IRD-rich, bioturbated sediments. We related the sedimentation in both sampled areas associated to steady environmental conditions with almost constant calving rates (absence of discrete IRD layers) and the presence of persistent bottom currents providing nutrients and oxygen to the benthic fauna. In both cores, however, the initial phase of MIS-2 contains an interval of laminated sediments with abundant, almost massive IRD. Coherently to the age model and radiocarbon dating, we correlate this interval to the Heinrich event H2 (Hemming, 2004).

5.2.4. Middle Weichselian Interglacial Stage (57–29 cal kyr BP)

The Middle Weichselian interglacial is characterized by bioturbated sediments with sparse IRD locally forming distinct centimeter-thick layers. The RPI curves of core GS191-01PC and core GS191-02PC show very similar trends in agreement with the global reference curve that presents a sharp minimum at ~40 kyr BP corresponding to a sharp peak to reverse (core GS191-01PC) or very low (core GS191-02PC) ChRM inclination (Figure 9). We linked this minimum with the Laschamps geomagnetic excursion (Kornprobst & Lénat, 2019), which in the studied cores spans a duration of about 1 kyr, in agreement with the observations made by Laj et al., (2004) and Channell (2006) for sediment core collected at high northern latitudes in the Atlantic. We reconstructed the virtual geomagnetic pole (VGP) path for the Laschamps excursion from the data of core GS191-01PC, where the Laschamps record appears better defined. The Laschamps VGP path traced a clockwise route, as shown in Figure 10. First, it moved southward over east Asia and middle Pacific longitudes then it moved down to southern Pacific Ocean and followed a northward directed path passing over eastern Africa and Europe (Figure 10). An analogous timing and VGP pattern was previously reported in other published records by Laj et al. (2006) and Channel (2006).

According to our age model, we associate the laminated, IRD-rich layer recovered at the base of core GS191-01PC (18.30–19.1 mbsf) to the Heinrich event H4 (38 cal kyr BP, Hamming, 2004). This interval is characterized by a significant positive peak in the various rock magnetic parameters indicating the presence of detritus rich in magnetic minerals.

In core GS191-02PC the Heinrich H4 event correspond is recorded with a few centimeter-thick laminated interval located between 10.6 and 10.8 mbsf that correspond to 37.5 and 38.9 cal kyr BP and located above the Laschamps magnetic anomaly (39–40 kyr BP). The Mono Lake geomagnetic excursion dated at ~33 kyr (Roberts, 2008), instead, has no evidence in our paleomagnetic curves. The lack of this excursion in our record could be due to sedimentary effects, related to the sedimentation rate and the processes that brings to the acquisition of sedimentary remanent magnetization (Roberts & Winklhofer, 2004), or to its possible occurrence at a depth corresponding to the break between consecutive u-channels, where paleomagnetic data from about 5 cm were discarded at each u-channel ends. In this stratigraphic subdivision, other intervals of massive IRD have been recognized, but none of them could confidentially be related to the Heinrich events H3 and H5.

5.2.5. Termination of the Middle Weichselian Glacial Stage (60–57 cal kyr BP)

According to the reconstructed age model, the age at the base of core GS191-02PC ranges between 57 and 60 cal kyr BP. Therefore, the laminated, IRD-rich sediments identified at the bottom at the core may record the Heinrich event H6 (~60 cal kyr BP, Hemming, 2004) located at the transition between the Middle Weichselian glacial stage MIS-4 and the interglacial stage MIS-3.

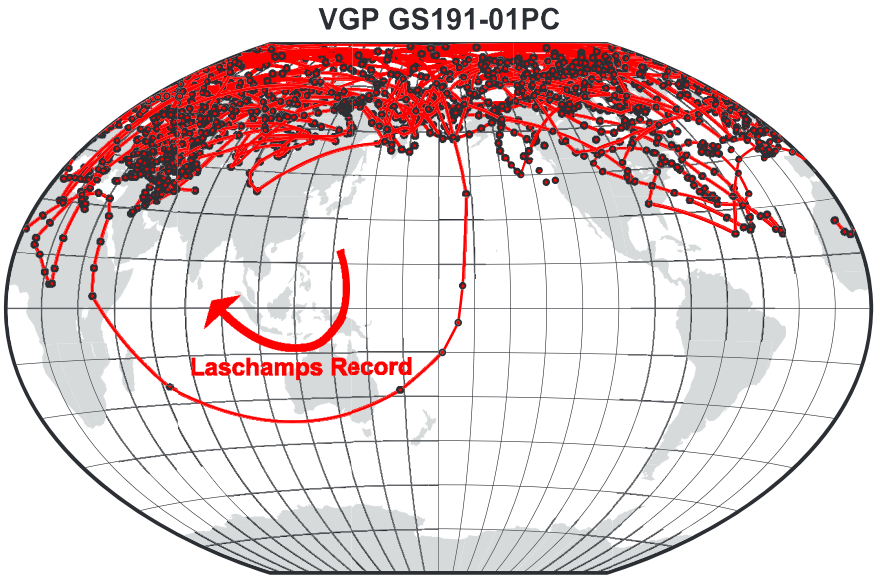

Figure 10. Virtual geomagnetic polar (VGP) paths for core GS191-01PC.

5.3. VGP Distribution

We analyzed the distribution of VGP calculated by individual ChRM directions under the assumption of a geocentric axial dipole (GAD) field, in order to analyze the PSV at high latitude and compare our data with model prediction (Model G by McElhinny & McFadden, 1997; TK03.GAD by Tauxe & Kent, 2004, and the model by Johnson et al., 2008). We computed the VGP scatter value expressed by the "*S*" parameter that indicates the angular standard deviation of the VGP distribution. Sharp and rapid geomagnetic features (such as the Laschamps excursion) and intervals affected by lithological changes (such as Heinrich events peaks) were disregarded since they are not considered to represent regular geomagnetic secular variation. Thus, we excluded data with large angular deviation, by using the iterative cutoff method proposed by Vandamme (1994; S_{cutoff}). The VGP scatter values (*S*) have been computed for the following intervals: Holocene, deglaciation phase after LGM, the MWP-1a and MWP-19ky, Late Weichselian glacial stage, and Middle Weichselian interglacial stage. In core GS191-01PC these intervals show relatively low *S* values, ranging from 13.2° and 17.2° with the exception of Late Weichselian glacial stage interval that reach an *S* value of 21.8 (Figures 11a–11c). For core GS191-02PC the obtained *S* values range from 11.8° and 17.7° (Figures 11d–11f).

The computed VGPs may have been affected by the arbitrary choices made in restoring paleomagnetic declination to fluctuate around geographic north, on average, and by sedimentary inclination shallowing. Whereas it is difficult to estimate the effect of arbitrary corrections to declination, the effect of the inclination shallowing should be to increase VGP scatter since the latter would be reduced for almost vertical paleomagnetic directions. The data indicate that the possible inclination shallowing is limited to ~5°. In any case, we report in the following some general remarks on the obtained VGP distributions. The VGP amplitude scatter obtained from both cores is generally lower that those predicted for high latitudes by various global geomagnetic time-averaged field models (Model G by McElhinny & McFadden, 1997; TK03.GAD by Tauxe & Kent, 2004, and Johnson et al., 2008) except for the deglaciation phase interval of Core GS191-01PC that fits well with Model G (Figure 11h). The models indicate an increase of *S* with the latitude, predicting *S* values of 19° and 23° according to TK03.GAD (when Vandamme cutoff is applied or not, respectively) or 21° according to model G and model by Johnson et al. (2008) at the latitude of PREPARED cores. Our results, although they provide *S* values lower than those predicted by the models, are, however, in general agreement with those observed in cores from nearby areas (e.g., Storfjorden trough, Sagnotti et al., 2011, 2016). Generally, the paleomagnetic data allow a reliable correlation with existing reference curves. At the same time, they indicate that the range of geomagnetic field variation, expressed as VGP scatter, has been relatively lower than that predicted at the same latitude from geomagnetic field models.

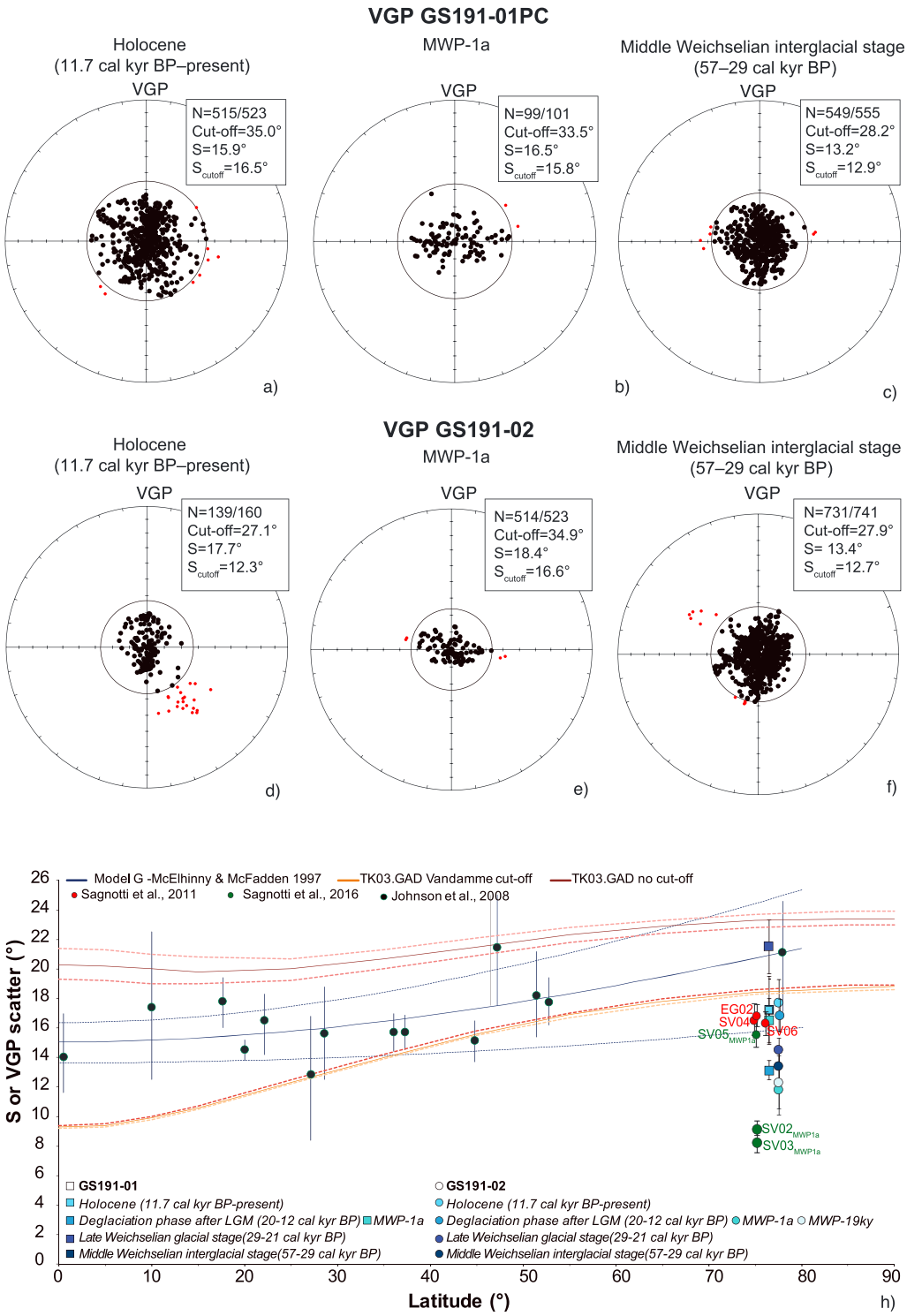

Figure 11. (a–f) Representative equal area plots computed for core GS191-01PC and core GS191-02PC. The small circles indicate the cutoff angle estimated by Vandamme (1994) method, and the red points indicate the discarded data according to such cutoff angle. For each core, the number (N) of data selected according to the Vandamme cutoff versus the total number of data and virtual geomagnetic polar (VGP) scatter with and without the Vandamme cutoff (S_{cutoff} and S) are also indicated; (g) VGP scatter values (S) of PREPARED cores, compared with the values from the PSV database of Johnson et al. (2008) for the last 5 Ma, including standard deviation bars, and with predictions according to the model G (McElhinny & McFadden, 1997) and the model TK03.GAD (Tauxe & Kent, 2004) computed with and without the cutoff criterion of Vandamme (1994) and with data from other sedimentary cores from the same area (Sagnotti et al., 2011, 2016).

6. Conclusions

Multiproxy lithostratigraphic and chronostratigraphic information allowed the reconstruction of a high-resolution age model for the studied depositional sequences located 200 km apart along the Western Spitsbergen margin. The downcore variation of magnetic parameters were chronologically tied by the 26 calibrated radiocarbon ages, the recognition of well constrained paleomagnetic features (e.g., the Laschamps geomagnetic excursion), and the identification of cryptotephra associated with dated volcanic events in the surrounding area. Cross-core correlation was furthermore constrained by the presence of an oxidized layer consistently observed along the margin and interpreted as a mark for the inception of deglaciation after LGM (Lucchi et al., 2013), and the presence of short living climatic events (i.e., Meltwater pulses and Heinrich events).

The high quality of paleomagnetic and rock magnetic data from PREPARED cores allowed a high-resolution correlation between the two long Calypso cores and a high-resolution match with the reference global PSV and RPI curves, specifically the SHA.DIF.14k (Pavón-Carrasco et al., 2014) and the GGF100k (Panovska et al., 2018) global magnetic models and the RPI stack GLOPIS-75 (Laj et al., 2004). We reconstructed the PSV of geomagnetic field back to 60 kyr BP, providing chronological constraints for reconstructing the age and rates of past depositional events that occurred in the continental slope of the Fram strait eastern margin during the latest major climatic changes. We distinguished four main stratigraphic intervals: the Holocene; the deglaciation phase after LGM; the Late Weichselian glacial stage, MIS-2; and the Middle Weichselian interglacial stage, MIS-3. Core GS191-02PC recovered at its base the termination of the Middle Weichselian glacial stage MIS-4.

The newly reconstructed age model allowed to identify characteristic stratigraphic marker beds such as the Meltwater pulse-1a and, for the first time in this area, the Meltwater pulse-19ky, whose initial emplacement was here better constrained to 19.8 cal kyr BP. Massive IRD deposits, locally laminated, were associated to the Heinrich events H1, H2, H4, and H6.

Two cryptotephra have been identified in the Holocene sequence. According to the age model and the chemical composition, such layers were related to the Suduroy tephra from the Katla volcano, Iceland, and to a newly recognized explosive event of the Jan Mayen volcano.

This study provides direct evidence of geomagnetic field dynamics at high latitude (76°–77°N) over the last 60,000 years. Both cores recovered the Laschamps magnetic excursion dated 39–41 kyr, never detected before at these high latitudes. The high-resolution record of the Laschamps geomagnetic polarity excursion suggests that this event had a duration of about 1 kyr and that related VGP path traced a clockwise route in agreement with that previously reported by Laj et al. (2006) and Channell (2006). The new paleomagnetic data indicate that the VGP scatter for the studied cores is lower than that predicted by the geomagnetic field models, in agreement with values formerly reported for the Holocene time interval (Sagnotti et al., 2011, 2016), extending the observation to the last 60 kyr BP. The database containing all metadata, raw data, and interpreted data is available for download as a supplementary publication (Caricchi et al., 2019).

Acknowledgments

The studied cores were collected within the Euroflees-2 PREPARED project. We would like to acknowledge the program Eurofleets-2 for giving the opportunity to run our research program through ship time dedication. We acknowledge John Hugo Johnson and crew of the G. O. Sars expedition 191 for dedication and competence during all acquisition activities and in particular Dag Inge Blindheim and Åse Sudman in charge for the Calypso coring acquisition. Sediment analyses were supported by the Italian projects PNRA-CORIBAR-IT (PdR 2013/C2.01) and Premiale ARCA (grant n.25_11_2013_973); and by the Spanish project DEGLABAR (CTM2010-17386) funded by the "Ministerio de Economia y Competitividad". All data presented in this paper are published with a DOI via GFZ Data Services (Caricchi et al., 2019) and can also be downloaded from the Thematic Core Service "Multi-scale laboratories" (https://epos-msl.uu.nl/dataset) of the European Plate Observing System (EPOS). We thank Sanja Panovska for providing the data of their global geomagnetic model. Stefanie Brachfeld and F. Javier Pavón-Carrasco are kindly acknowledged for the precious suggestions that highly contributed to improve the paper. We also thank Josh Feinberg for the careful editorial handling.

References

Banerjee, S. K., King, J., & Marvin, J. (1981). A rapid method for magnetic granulometry with applications to environmental studies. *Geophysical Research Letters*, *8*(4), 333–336. https://doi.org/10.1029/GL008i004p00333

Barletta, F., St-Onge, G., Channel, J. E. T., & Darby, D. A. (2008). High resolution paleomagnetic secular variation and relative paleointensity records from the western Canadian Arctic: Implication for Holocene stratigraphy and geomagnetic field behavior. *Canadian Journal of Earth Sciences*, *45*(11), 1265–1281. https://doi.org/10.1139/E08-039

Blanchet, C. L., Thouveny, N., Vidal, L., Leduc, G., Tachikawa, K., Bard, E., & Beaufort, L. (2007). Terrigenous input response to glacial/interglacial climatic variations over southern Baja California: A rock magnetic approach. *Quaternary Science Reviews*, *26*(25-28), 3118–3133. https://doi.org/10.1016/j.quascirev.2007.07.008

Bondevik, S., Mangerud, J., Birks, H. H., Gulliksen, S., & Reimer, P. (2006). Changes in North Atlantic radiocarbon reservoir ages during the Allerød and Younger Dryas. *Science*, *312*(5779), 1514–1517. https://doi.org/10.1126/science.1123300

Brachfeld, S., Barletta, F., St-Onge, G., Darby, D., & Ortiz, J. D. (2009). Impact of diagenesis on the environmental magnetic record from a Holocene sedimentary sequence from the Chukchi–Alaskan margin, Arctic Ocean. *Global and Planetary Change*, *68*(1-2), 100–114. https://doi.org/10.1016/j.gloplacha.2009.03.023

Brachfeld, S. A. (2006). High-field magnetic susceptibility (χHF) as a proxy of biogenic sedimentation along the Antarctic Peninsula. *Physics of the Earth and Planetary Interiors*, *156*(3-4), 274–282. https://doi.org/10.1016/j.pepi.2005.06.019

Brachfeld, S. A., Banerjee, S. K., Guyodo, Y., & Acton, G. D. (2002). A 13,200 year history of century to millennial scale paleoenvironmental change magnetically recorded in the Palmer Deep, western Antarctic Peninsula. *Earth and Planetary Science Letters*, *194*(3-4), 311–326. https://doi.org/10.1016/S0012-821X(01)00567-2

Butt, F. A., Elverhøi, A., Solheim, A., & Forsberg, C. F. (2000). Deciphering late Cenozoic evolution of the western Svalbard Margin based of ODP Site 986 results. *Marine Geology*, *169*(3-4), 373–390. https://doi.org/10.1016/S0025-3227(00)00088-8

Carbonara, K., Mezgec, K., Varagona, G., Musco, M. E., Lucchi, R. G., Villa, G., et al. (2016). Palaeoclimatic changes in Kveithola, Svalbard, during the Late Pleistocene deglaciation and Holocene: Evidences from microfossil and sedimentary records. *Palaeogeography Palaeoclimatology Palaeoecology*, *463*, 136–149. https://doi.org/10.1016/j.palaeo.2016.10.003

Caricchi, C., Lucchi, R.G., Sagnotti, L., Macrì, P., Di Roberto, A., Del Carlo, P., et al. (2019). Data supplement to: A high-resolution geomagnetic relative paleointensity record from the Arctic Ocean deep water gateway deposits during the last 60 ky. GFZ Data Services. http://doi.org/10.5880/FIDGEO.2019.011

Caricchi, C., Lucchi, R. G., Sagnotti, L., Macrì, P., Morigi, C., Melis, R., et al. (2018). Paleomagnetism and rock magnetism from sediments along a continental shelf-to-slope transect in the NW Barents Sea: Implications for geomagnetic and depositional changes during the past 15 thousand years. *Global and Planetary Change*, *160*, 10–27. https://doi.org/10.1016/j.gloplacha.2017.11.007

Chambers, F. M., Daniell, J. R. G., Hunt, J. B., Molloy, K., & O'Connell, M. (2004). Tephrostratigraphy of An Loch Mor, InisOirr, western Ireland: Implications for Holocene tephrochronology in the northeastern Atlantic region. *The Holocene*, *14*(5), 703–720. https://doi.org/10.1191/0959683604hl749rp

Channell, J. E. T. (2006). Late Brunhes polarity excursions (Mono Lake, Laschamp, Iceland Basin and Pringle Falls) recorded at ODP Site 919 (Irminger Basin). *Earth and Planetary Science Letters*, *244*(1-2), 378–393. https://doi.org/10.1016/j.epsl.2006.01.021

Clark, P. U., McCabe, A. M., Mix, A. C., & Weaver, A. J. (2004). Rapid rise of sea level 19,000 years ago and its global implications. *Science*, *304*(5674), 1141–1144. https://doi.org/10.1126/science.1094449

Eiken, O., & Hinz, K. (1993). Contourites in the Fram Strait. *Sedimentary Geology*, *82*(1-4), 15–32. https://doi.org/10.1016/0037-0738(93)90110-Q

Faleide, J. I., Solheim, A., Fiedler, A., Hjelstuen, B. O., Andersen, E. S., & Vanneste, K. (1996). Late Cenozoic evolution of the western Barents Sea-Svalbard continental margin. *Global and Planetary Change*, *12*(1-4), 53–74. https://doi.org/10.1016/0921-8181(95)00012-7

Fu, Y., von Dobeneck, T., Franke, C., Heslop, D., & Kasten, S. (2008). Rockmagnetic identification and geochemical process models of greigite formation in Quaternary marine sediments from the Gulf of Mexico (IODP Hole U1319A). *Earth and Planetary Science Letters*, *275*(3-4), 233–245. https://doi.org/10.1016/j.epsl.2008.07.034

Guyodo, Y., & Valet, J.-P. (1999). Global changes in geomagnetic intensity during the past 800 thousand years. *Nature*, *399*(6733), 249–252. https://doi.org/10.1038/20420

Hemming, S. R. (2004). Heinrich events: Massive late Pleistocene detritus layers of the North Atlantic and their global climate imprint. *Reviews of Geophysics*, *42*, RG1005. https://doi.org/10.1029/2003RG000128

Hounslow, M. W., & Morton, A. C. (2004). Evaluation of sediment provenance using magnetic mineral inclusions in clastic silicates: Comparison with heavy mineral analysis. *Sedimentary Geology*, *171*(1-4), 13–36. https://doi.org/10.1016/j.sedgeo.2004.05.008

Housley, R. A., Lane, C. S., Cullen, V. L., Weber, M.-J., Riede, F., Gamble, C. S., & Brock, F. (2012). Icelandic volcanic ash from the Late-glacial open-air archaeological site of Ahrenshöft LA 58 D, North Germany. *Journal of Archaeological Science*, *39*(3), 708–716. https://doi.org/10.1016/j.jas.2011.11.003

Imsland, P. (1984). Petrology, mineralogy and evolution of the Jan Mayen magma system. *VisindafelagIslendinga, Reykjavik*, 43, 332.

Irvine, T. N., & Baragar, W. R. A. (1971). A guide to the chemical classification of the common volcanic rocks. *Canadian Journal of Earth Sciences*, *8*(5), 523–548. https://doi.org/10.1139/e71-055

Jakobsson, M., Backman, J., Rudels, B., Nycander, J., Frank, M., Mayer, L., et al. (2007). The early Miocene onset of a ventilated circulation regime in the Arctic Ocean. *Nature*, *447*(7147), 986–990. https://doi.org/10.1038/nature05924

Jennings, A., Thordarson, T., Zalzal, K., Stoner, J., Hayward, C., Geirsdottir, A., & Miller, G. (2014). Holocene tephra from Iceland and Alaska in SE Greenland shelf sediments. In W. E. N. Austin, P. M. Abbott, S. M. Davies, N. J. G. Pearce, & S. Wastegard (Eds.), *Marine tephrochronology*, *The Geological Society of London, Special Publications* (Vol. 398, pp. 157–193). https://doi.org/10.1144/SP398.6

Johnson, C. L., Constable, C. G., Tauxe, L., Barendregt, R., Brown, L. L., Coe, S. S., et al. (2008). Recent investigations of the 0–5 Ma geomagnetic field recorded by lava flows. *Geochemistry, Geophysics, Geosystems*, *9*, Q04032. https://doi.org/10.1029/2007GC001696

Kissel, C., Laj, C., Clemens, S., & Solheid, P. (2003). Magnetic signature of environmental changes in the last 1.2 Myr at ODP Site 1146, South China. *Sea. Mar. Geol.*, *201*(1-3), 119–132. https://doi.org/10.1016/S0025-3227(03)00212-3

Kissel, C., Laj, C., Labeyrie, L., Dokken, T., Voelker, A., & Blamart, D. (1999). Rapid climatic variations during marine isotopic stage 3: Magnetic analysis of sediments from Nordic seas and North Atlantic. *Earth and Planetary Science Letters*, *171*(3), 489–502. https://doi.org/10.1016/S0012-821X(99)00162-4

Kissel, C., Laj, C., Lehman, B., Labyrie, L., & Bout-Roumazeilles, V. (1997). Changes in the strength of the Iceland–Scotland overflow water in the last 200,000 years: Evidence from magnetic anisotropy analysis of core SU90-33. *Earth and Planetary Science Letters*, *152*(1-4), 25–36. https://doi.org/10.1016/S0012-821X(97)00146-5

Kissel, C., Laj, C., Piotrowski, A. M., Goldstein, S. L., & Hemming, R. S. (2008). Millennial-scale propagation of Atlantic deep waters to the glacial Southern Ocean. *Paleoceanography*, *23*, PA2102. https://doi.org/10.1029/2008PA001624

Kornprobst, J., & Lénat, J. F. (2019). Changing name for Earth's changing poles. *Eos*, *100*. https://doi.org/10.1029/2019EO117913

Kotilainen, A. T., Saarinen, T., & Winterhalter, B. (2000). High-resolution paleomagnetic dating of sediments deposited in the central Baltic Sea during the last 3000 years. *Marine Geology*, *166*(1-4), 51–64. https://doi.org/10.1016/S0025-3227(00)00012-8

Laj, C., Kissel, C., & Beer, J. (2004). In J. E. T. Channel, D. V. Kent, W. Lowrie, & J. G. Meert (Eds.), *High resolution global paleointensity stack since 75 kyr (GLOPIS-75) calibrated to absolute values*, *Timescales of the paleomagnetic field geophysical monograph series*, (145th ed.). Washington D.C.: American Geophysical Union. https://doi.org/10.1029/145GM19

Laj, C., Kissel, C., Mazaud, A., Channell, J. E. T., & Beer, J. (2000). North Atlantic paleointensity stack since 75 ka (NAPIS-75) and the duration of the Laschamp event. *Philosophical Transactions of the Royal Society*, Series A, *358*, 1009–1025.

Laj, C., Kissel, C., & Roberts, A. P. (2006). Geomagnetic field behavior during the Icelandic basin and Laschamp geomagnetic excursions: A simple transitional field geometry? *Geochemistry, Geophysics*, *7*(3), Q03004. https://doi.org/10.1029/2005GC001122

Larsen, G., Newton, A. J., Dugmore, A. J., & Vilmundardottir, E. G. (2001). Geochemistry, dispersal, volumes and chronology of Holocene silicic tephra layers from the Katla volcanic system, Iceland. *Journal of Quaternary Science*, *16*(2), 119–132. https://doi.org/10.1002/jqs.587

Le Bas, M. J., Le Maitre, R. W., Streckeisen, A., & Zanettin, B. (1986). A chemical classification of volcanic rocks based on the total alkali-silica diagram. *Journal of Petrology*, *27*(3), 745–750. https://doi.org/10.1093/petrology/27.3.745

Lisé-Pronovost, A., St-Onge, G., Brachfeld, S., Barletta, F., & Darby, D. (2009). Paleomagnetic constraints on the Holocene stratigraphy of the Arctic Alaskan margin. *Global and Planetary Change*, *68*(1-2), 85–99. https://doi.org/10.1016/j.gloplacha.2009.03.015

Liu, Q., Roberts, A. P., Larrasoaña, J. C., Banerjee, S. K., Guyodo, Y., Tauxe, L., & Oldfield, F. (2012). Environmental magnetism: Principles and applications. *Reviews of Geophysics*, *50*, RG4002. https://doi.org/10.1029/2012RG000393

Lucchi, R. G., Camerlenghi, A., Rebesco, M., Colmenero-Hidalgo, E., Sierro, F. J., Sagnotti, L., et al. (2013). Postglacial sedimentary processes on the Storfjorden and Kveithola trough mouth fans: Significance of extreme glacimarine sedimentation. *Global and Planetary Change*, *111*, 309–326. https://doi.org/10.1016/j.gloplacha.2013.10.008

Lucchi, R.G., Kovacevic, V., Aliani, S., Caburlotto, A., Celussi, M., Corgnati, L., et al. (2014). PREPARED: Present and past flow regime on contourite drifts west of Spitsbergen. EUROFLEETS-2 Cruise Summary Report, R/V G.O. Sars Cruise No. 191, 05/06/2014–15/06/2014, Tromsø – Tromsø (Norway), 89pp.

Lucchi, R. G., Sagnotti, L., Camerlenghi, A., Macrì, P., Pedrosa, M. T., & Giorgetti, G. (2015). Marine sedimentary record of Meltwater Pulse 1a along the NW Barents Sea continental margin. *Arktos*, *1*(1), 7. https://doi.org/10.1007/s41063-015-0008-6

Maher, B. A. (1988). Magnetic properties of some synthetic sub-micron magnetites. *Geophysical Journal of the Royal Astronomical Society*, *94*(1), 83–96. https://doi.org/10.1111/j.1365-246X.1988.tb03429.x

Mangerud, J., Bondevik, S., Gulliksen, S., Hufthammerd, A. K., & Høisætere, T. (2006). Marine ^{14}C reservoir ages for 19th century whales and molluscs from the North Atlantic. *Quaternary Science Reviews*, *25*(23-24), 3228–3245. https://doi.org/10.1016/j.quascirev.2006.03.010

Mattingsdal, R., Knies, J., Andreassen, K., Fabian, K., Husum, K., Grøsfjeld, K., & De Schepper, S. (2014). A new 6 Myr stratigraphic framework for the AtlanticeArctic Gateway. *Quaternary Science Reviews*, *92*, 170–178. https://doi.org/10.1016/j.quascirev.2013.08.022

Mazaud, A., Sicre, M. A., Ezat, U., Pichon, J. J., Duprat, J., Laj, C., et al. (2002). Geomagnetic-assisted stratigraphy and sea surface temperature changes in core MD94-103 (Southern Indian Ocean): Possible implications for North-South climatic relationships around H4. *Earth and Planetary Science Letters*, *201*, 159–170. https://doi.org/10.1016/S0012-821X(02)00662-3

McElhinny, M. W., & McFadden, P. L. (1997). Palaeosecular variation over the past 5 Myr based on a new generalized database. *Geophysical Journal International*, *131*(2), 240–252. https://doi.org/10.1111/j.1365-246X.1997.tb01219.x

Óladóttir, B. A., Sigmarsson, O., Larsen, G., & Thordarson, T. (2008). Katla volcano, Iceland: Magma composition, dynamics and eruption frequency as recorded by Holocene tephra layers. *Bulletin of Volcanology*, *70*(4), 475–493. https://doi.org/10.1007/s00445-007-0150-5

Panovska, S., Constable, C. G., & Korte, M. (2018). Extending global continuous geomagnetic field reconstructions on timescales beyond human civilization. *Geochemistry, Geophysics, Geosystems*, *19*, 4757–4772. https://doi.org/10.1029/2018gc007966

Patton, H., Hubbard, A., Andreassen, K., Auriac, A., Whitehouse, P. L., Stroeven, A. P., et al. (2017). Deglaciation of the Eurasian ice sheet complex. *Quaternary Science Reviews*, *169*, 148–172. https://doi.org/10.1016/j.quascirev.2017.05.019

Pavón-Carrasco, F. J., Osete, M. L., Torta, J. M., & De Santis, A. (2014). A geomagnetic field model for the Holocene based on archeomagnetic and lava flow data. *Earth and Planetary Science Letters*, *388*, 98–109. https://doi.org/10.1016/j.epsl.2013.11.046

Pilcher, J., Bradley, R. S., Francus, P., & Anderson, L. (2005). A Holocene tephra record from the Lofoten Islands, Arctic Norway. *Boreas*, *34*(2), 136–156. https://doi.org/10.1080/03009480510012935

Poirier, A., & Hillaire-Marcel, C. (2011). Improved Os-isotope stratigraphy of the Arctic Ocean. *Geophysical Research Letters*, *38*, L14607. https://doi.org/10.1029/2011GL047953

Rebesco, M., Camerlenghi, A., & Van Loon, A. J. (2008). Contourite research: A field in full development. In M. Rebesco, & A. Camerlenghi (Eds.), *Contourites. Developments in sedimentology* (Vol. 60, pp. 1–10).

Rebesco, M., Wåhlin, A., Laberg, J. S., Schauer, U., Beszczynska-Möller, A., Lucchi, R. G., et al. (2013). Quaternary Contourite drifts of the Western Spitsbergen margin. *Deep Sea Research Part I: Oceanographic Research Papers*, *79*, 156–168. https://doi.org/10.1016/j.dsr.2013.05.013

Reimer, P. (2013). IntCal13 and Marine13 radiocarbon age calibration curves 0–50,000 years cal BP. *Radiocarbon*, *55*(04), 1869–1887. https://doi.org/10.2458/azu_js_rc.55.16947

Roberts, A. P. (2008). Geomagnetic excursions: Knowns and unknowns. *Geophysical Research Letters*, *35*, L17307. https://doi.org/10.1029/2008GL034719

Roberts, A. P., Sagnotti, L., Florindo, F., Bohaty, S. M., Verosub, K. L., Gary, S. W., & Zachos, J. C. (2013). Environmental magnetic record of paleoclimate, unroofing of the Transantarctic Mountains, and volcanism in late Eocene to early Miocene glaci-marine sediments from the Victoria Land Basin, Ross Sea, Antarctica. *Journal of Geophysical Research: Solid Earth*, *118*, 1845–1861. https://doi.org/10.1002/jgrb.50151

Roberts, A. P., & Winklhofer, M. (2004). Why are geomagnetic excursions not always recorded in sediments? Constraints from post-depositional remanent magnetization lock-in modelling. *Earth and Planetary Science Letters*, *227*(3-4), 345–359. https://doi.org/10.1016/j.epsl.2004.07.040

Rousse, S., Kissel, C., Laj, C., Eiríksson, J., & Knudsen, K.-L. (2006). Holocene centennial to millennial-scale climatic variability: Evidence from high-resolution magnetic analyses of the last 10 cal kyr off North Iceland (core MD99-2275). *Earth and Planetary Science Letters*, *242*(3-4), 390–405. https://doi.org/10.1016/j.epsl.2005.07.030

Sagnotti, L. (2013). Demagnetization Analysis in Excel (DAIE)—An open source workbook in Excel for viewing and analyzing demagnetization data from paleomagnetic discrete samples and u-channels. *Annales de Geophysique*, *56*, D0114. https://doi.org/10.4401/ag-6282

Sagnotti, L., & Caricchi, C. (2018). StratFit: An excel workbook for correlation of multiple stratigraphic trends. *Annales de Geophysique*, *61*(3), DA341. https://doi.org/10.4401/ag-7619

Sagnotti, L., Macrì, P., Lucchi, R., Rebesco, M., & Camerlenghi, A. (2011). A Holocene paleosecular variation record from the northwestern Barents Sea continental margin. *Geochemistry, Geophysics*, *12*(11), Q11Z33. https://doi.org/10.1029/2011GC003810

Sagnotti, L., Macrì, P., & Lucchi, R. G. (2016). Geomagnetic paleosecular variation around 15 ka ago from NW Barents Sea cores (south of Svalbard). *Geophysical Journal International*, *204*(2), 785–797. https://doi.org/10.1093/gji/ggv485

Stoner, J. S., & Andrews, J. T. (1999). The North Atlantic as a Quaternary magnetic archive. In B. Maher & R. Thompson (Eds.), *Quaternary climates, environments and magnetism* (pp. 49–80). Cambridge: Cambridge University Press. https://doi.org/10.1017/CBO9780511535635.003

Stoner, J. S., Channell, J. E. T., Hillaire-Marcel, C., & Kissel, C. (2000). Geomagnetic paleointensity and environmental record from Labrador Sea core MD95-2024: Global marine sediment and ice core chronostratigraphy for the last 110 kyr. *Earth and Planetary Science Letters*, *183*(1-2), 161–177. https://doi.org/10.1016/S0012-821X(00)00272-7

Stoner, J. S., Jennings, A., Kristjánsdóttir, G. B., Dunhill, G., Andrews, J. T., & Hardardóttir, J. (2007). A paleomagnetic approach toward refining Holocene radiocarbon-based chronologies: Paleoceanographic records from the north Iceland (MD99-2269) and east Greenland (MD99-2322) margins. *Paleoceanography*, *22*, PA1209. https://doi.org/10.1029/2006PA001285

Stoner, J. S., Laj, C., Channell, J. E. T., & Kissel, C. (2002). South Atlantic and North Atlantic geomagnetic paleointensity stacks (0–80 ka): Implications for inter-hemispheric correlation. *Quaternary Science Reviews*, *21*(10), 1141–1151. https://doi.org/10.1016/S0277-3791(01)00136-6

St-Onge, G., Stoner, J. S., & Hillaire-Marcel, C. (2003). Holocene paleomagnetic records from the St. Lawrence Estuary, eastern Canada: Centennial- to millennial-scale geomagnetic modulation of cosmogenic isotopes. *Earth and Planetary Science Letters*, *209*(1-2), 113–130. https://doi.org/10.1016/S0012-821X(03)00079-7

Stuiver, M., & Reimer, P. J. (1993). Extended 14C data base and revised CALIB 3.0 ^{14}C age calibration program. *Radiocarbon*, *35*(01), 215–230. https://doi.org/10.1017/S0033822200013904

Tauxe, L. (1993). Sedimentary records of relative paleointensity of the geomagnetic field: Theory and practice. *Reviews of Geophysics*, *31*(3), 319–354. https://doi.org/10.1029/93RG01771

Tauxe, L., & Kent, D. (2004). A simplified statistical model for the geomagnetic field and the detection of shallow bias in paleomagnetic inclinations: Was the ancient magnetic field dipolar? In J. E. T. Channell, et al. (Eds.), *Timescales of the Internal Geomagnetic Field*, *Geophys. Monogr. Ser. 145* (pp. 101–115). Washington, D. C.: American Geophysical Union.

Telford, R. J., Heegaard, E., & Birks, H. J. (2004). The intercept is a poor estimate of a calibrated radiocarbon age. *The Holocene*, *14*(2), 296–298. https://doi.org/10.1191/0959683604hl707fa

Thompson, R., & Oldfield, F. (1986). *Environmental magnetism*. London: Allen & Unwin: Springer. https://doi.org/10.1007/978-94-011-8036-8

Valet, J.-P., & Meynadier, L. (1993). Geomagnetic field intensity and reversals during the past four million years. *Nature*, *366*(6452), 234–238. https://doi.org/10.1038/366234a0

Vandamme, D. (1994). A new method to determine paleo-secular variation. *Physics of the Earth and Planetary Interiors*, *85*(1-2), 131–142. https://doi.org/10.1016/0031-9201(94)90012-4

Verosub, K. L., & Roberts, A. P. (1995). Environmental magnetism: Past, present, and future. *Journal of Geophysical Research*, *100*, 2175–2192.

Vorren, T. O., & Laberg, J. S. (1997). Trough mouth fans—Palaeoclimate and ice-sheet monitors. *Quaternary Science Reviews*, *16*(8), 865–881. https://doi.org/10.1016/S0277-3791(97)00003-6

Wastegård, S. (2002). Early to middle Holocene silicic tephra horizons from the Katla volcanic system, Iceland: New results from the Faroe Islands. *Journal of Quaternary Science*, *17*(8), 723–730. https://doi.org/10.1002/jqs.724

Yamazaki, T., & Oda, H. (2005). A geomagnetic paleointensity stack between 0.8 and 3.0 Ma from equatorial Pacific sediment cores. *Geochemistry, Geophysics, Geosystems*, *6*, Q11H20. https://doi.org/10.1029/2005GC001001